USGS
science for a changing world

Prepared in cooperation with the U.S. Air Force

Seismic Images and Subsurface Structures of Northeastern Edwards Air Force Base, Kern County, California

Open-File Report 2023–1018

U.S. Department of the Interior
U.S. Geological Survey

Seismic Images and Subsurface Structures of Northeastern Edwards Air Force Base, Kern County, California

By Rufus D. Catchings, Mark R. Goldman, Joanne H. Chan, Robert R. Sickler, and Coyn J. Criley

Prepared in cooperation with the U.S. Air Force

Open-File Report 2023–1018

U.S. Department of the Interior
U.S. Geological Survey

U.S. Geological Survey, Reston, Virginia: 2023

Suggested citation:
Catchings, R.D., Goldman, M.R., Chan, J.H., Sickler, R.R., and Criley, C.J., 2023, Seismic images and subsurface structures of northeastern Edwards Air Force Base, Kern County, California: U.S. Geological Survey Open-File Report 2023–1018, 29 p., https://doi.org/10.3133/ofr20231018.

Associated data for this publication:
Goldman, M.R., Catchings, R.D., Chan, J.H., Criley, C.J., and Sickler, R.R., 2021, Data release for a 2020 high-resolution seismic survey across northeastern Edwards Air Force Base, Kern County, California: U.S. Geological Survey data release, https://doi.org/10.5066/P9ZAM79S.

ISSN 2331-1258 (online)

Acknowledgments

We thank Peter Robles of Edwards Air Force Base for access. Funding was provided by the U.S. Air Force, the U.S. Geological Survey (USGS) Earthquake Hazards Program, and the USGS Earthquake Science Center in Moffett Field, California. This work was done in collaboration with the USGS Water Resources Discipline.

We thank USGS scientist Garet J. Huddleston and USGS volunteers Nathan Suits and Sara Ray for assistance in acquiring the data for this report. We thank Nicole Fenton (USGS) for discussions and well data. We thank Walter Mooney and Josie Nevitt (USGS) for reviewing the manuscript.

Contents

Figures

Tables

Conversion Factors

U.S. customary units to International System of Units

Multiply	By	To obtain
	Length	
foot (ft)	0.3048	meter (m)
	Mass	
pound, avoirdupois (lb)	0.4536	kilogram (kg)

International System of Units to U.S. customary units

Multiply	By	To obtain
	Length	
centimeter (cm)	0.3937	inch (in.)
meter (m)	3.281	foot (ft)
kilometer (km)	0.6214	mile (mi)
meter (m)	1.094	yard (yd)
	Flow rate	
meter per second (m/s)	3.281	foot per second (ft/s)
	Mass	
kilogram (kg)	2.205	pound avoirdupois (lb)

Datum

Vertical coordinate information is referenced to the topographically lowest point along the seismic profile, which is 2,595.5 feet above sea level as referenced to the World Geodetic System of 1984 (WGS 84).

Abbreviations

1D	one-dimensional
2D	two-dimensional
AFB	Air Force Base
AGC	automatic gain control
AWD	accelerated weight drop
CDP	common depth point
GPS	Global Positioning System
LVZ	low-velocity zone
MASW	multichannel analysis of surface waves
NMO	normal moveout
μ	Poisson's ratio
P-wave	compressional-wave
S-wave	shear-wave
TCE	trichloroethylene
v_P	compressional-wave (P-wave) velocity
v_S	shear-wave (S-wave) velocity
v_P/v_S ratio	ratio of compressional-wave (P-wave) velocity to shear-wave (S-wave) velocity
USGS	U.S. Geological Survey
~	approximately
>	greater than
<	less than

Seismic Images and Subsurface Structures of Northeastern Edwards Air Force Base, Kern County, California

By Rufus D. Catchings, Mark R. Goldman, Joanne H. Chan, Robert R. Sickler, and Coyn J. Criley

Abstract

We used multi-component seismic data (including two-dimensional images of compressional-wave velocity [v_P], shear-wave velocity [v_S], the ratio of compressional-wave velocity to shear-wave velocity [v_P/v_S ratio], Poisson's ratio [μ], and seismic reflections) along a transect across northeastern Edwards Air Force Base to investigate the upper few hundred meters of the subsurface. The shallow subsurface there is characterized by unconsolidated sediments (v_P of less than 2,500 meters per second [m/s]; v_S of less than 1,500 m/s) in the upper 40 meters (m), underlain by weathered granitic basement rock (v_P of 2,500–4,000 m/s; v_S of 1,500–2,700 m/s) to about 100 m depth and unweathered granitic basement rock (v_P of 4,000–6,000 m/s; v_S of 2,700–4,000 m/s). The depth to basement rock varies laterally along the transect by as many as tens of meters. The top of groundwater, as indicated by both the 1,500-m/s v_P contour and measurements in five wells along the transect, is located 8–30 m below the surface. In places, the top of groundwater is vertically offset over short lateral distances, likely the result of fault barriers. Faults mapped at the surface along the northeastern part of the transect correlate with multiple seismic indicators of faulting at the same locations. These same indicators show evidence for faulting in several other places along the transect beneath the alluvium. A major zone of faulting is apparent near the center of the seismic profile and is characterized by offsets in the top of groundwater; diffractions on the reflection image; a near-vertical zone of low v_S; a corresponding near-vertical, shallow-depth zone of high v_P relative to adjacent rocks (indicating high saturation); a near-vertical zone of high v_P/v_S ratios; and a near-vertical zone of high Poisson's ratios (also indicating saturation). Many of these anomalies extend at least 400 m deep, reaching into granitic basement rock and indicating that the fault zone is water-saturated to those depths. There is likely vertical flow of contaminants along these fault zones, which are apparently barriers to the lateral flow of groundwater. The major central fault zone marks a boundary beyond which contaminant flow is apparently impeded. Along the southwestern part of the transect, there are also areas with similar indicators of faulting, but these appear to be smaller fault zones.

Introduction

The U.S. Geological Survey (USGS) conducted a multi-component seismic imaging survey in the northeastern section of Edwards Air Force Base (AFB) in June 2020 (fig. 1*A*), referred to here as the Edwards seismic profile. Our objectives were to evaluate features of the subsurface, including the top of groundwater, shallow subsurface lithology, and subsurface faults, which likely affect groundwater and associated contaminant flow in the area. Faults have been mapped in the region and in the immediate study area (Dibblee, 1967; Bortugno, 1986; Jennings, 1994; Bryant; 2002; Hart and others, 1988; Bryant, 2017; Cyr and Miller, 2023) of the Edwards seismic profile (fig. 1*B*). Subsurface characteristics have been evaluated from numerous wells in the area (Earth Tech Inc., 2006), but the complexity of the subsurface makes it difficult to laterally extrapolate observations between individual wells. In this study, we used seismic imaging techniques to evaluate various subsurface characteristics over longer linear distances that connect several wells and beyond.

Methodology and Background Information

In this study, we used multiple seismic methods to evaluate subsurface stratigraphy, lithology, faulting, and groundwater variations. These methods include compressional-wave (P-wave) refraction tomography to develop P-wave velocity (v_P) models, multichannel analysis of surface waves (MASW) to develop a shear-wave (S-wave) velocity (v_S) model, v_P/v_S and Poisson's ratio (μ) models developed from our v_P and v_S models, and P-wave seismic reflection imaging. We combined the images and models from these separate analyses and compared them with other data, such as water-well data and geologic

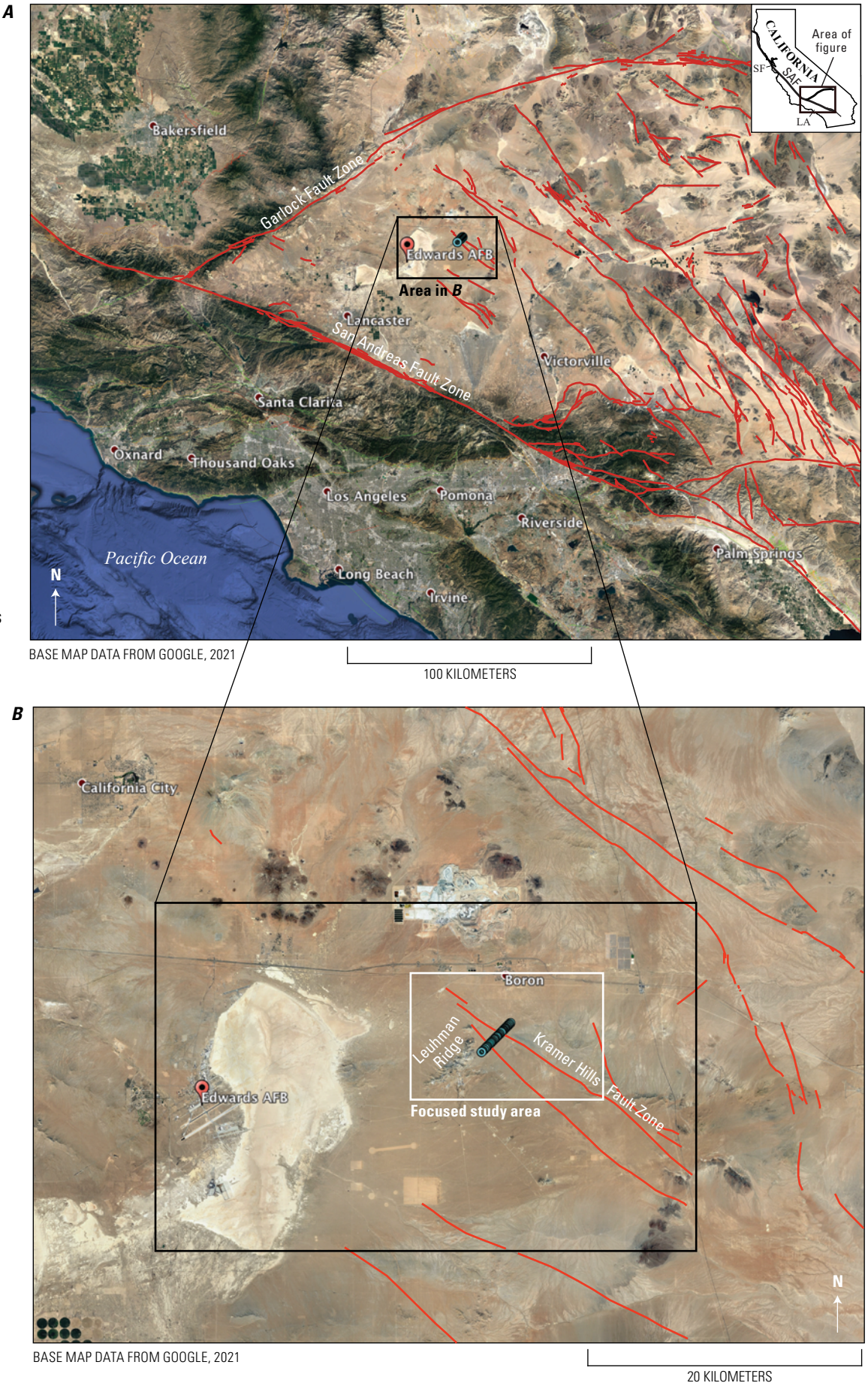

Figure 1. Satellite image of the wider region around the study area and the location of the seismic profile within the study area at Edwards Air Force Base, southern California. *A*, Satellite image of the greater Los Angeles area and the Mojave Desert region. Undifferentiated faults are shown as red lines, including those of the San Andreas and Garlock Fault Zones, between which our study area at Edwards Air Force Base is located (rectangle). The Edwards seismic profile is shown with light-blue-colored circles. *B*, Satellite image of the northeastern part of Edwards Air Force Base. The large rectangle shows the location of the rectangle from part *A*, and the smaller rectangle shows our focused study area. The light-blue-colored circles show the location of the Edwards seismic profile. Red lines show inferred Quaternary faults (Bryant, 2017). SF, San Francisco; LA, Los Angeles; SAF, San Andreas Fault Zone; AFB, Air Force Base.

maps. These combined seismic methods are useful in mapping lateral variations in groundwater, identifying and locating subsurface faults, and differentiating among various subsurface lithologies and physical conditions, such as water saturation and weathering. In the next section, we briefly describe these seismic methods and explain why they provide such information.

Groundwater Mapping and Stratigraphic Identification

P-wave refraction tomography is useful in mapping lateral variations in groundwater within sediments. High-resolution P-wave tomography studies (with corresponding well data) show that v_P of 1,500 meters per second (m/s) strongly correlates with the top of groundwater in near-surface sediments (for example, Catchings and others, 1999a, b, 2000, 2001a, b, 2006, 2007, 2008, 2009, 2010, 2013, 2014; Gandhok and others, 1999; Christensen and others, 2015; Rosa and others, 2016). Such tomographic studies also show that sediments with v_P of approximately 2,800–3,000 m/s generally correlate with geologic materials that are too dense to form productive aquifers, such as low-porosity sedimentary rocks or weathered crystalline rocks. P-wave velocity can also be used to differentiate between unconsolidated sediments and crystalline (basement) rocks. Competent (unweathered) granitic rocks typically have v_P between 4,000 m/s and 6,000 m/s in the shallow crust (Zappe, 1979; Catchings and others, 1999a, b, 2000, 2002; Holbrook and others, 2014; Sowers and Boyd, 2019), but weathered granitic rocks in the upper few hundred meters of the crust may have v_P values as low as 2,500 m/s (Zappe, 1979). S-wave velocities can indicate competent crystalline rocks as well; v_S typically varies by rock type, but for competent granitic rocks in the upper few hundred meters of the crust in the Mojave Desert, v_S normally exceeds approximately (~) 1,700 m/s (Zappe, 1979). However, weathering, shearing, and lack of compaction can decrease the v_S of shallow granitic rocks to less than (<) 1,000 m/s (see for example, Fumal, 1978; Olona and others, 2010; Catchings and others, 2020).

High v_P/v_S ratios (greater than [>] 2.0) are expected in water-saturated, unconsolidated sediments; v_P is typically 1,500 m/s or greater and v_S is typically low (~600 m/s or less) in unconsolidated sediments (Fumal, 1978; Catchings and others, 2014). Although the actual v_S value varies on the basis of the composition, compaction, and to a lesser extent, degree of saturation of the unconsolidated sediments, v_S will still be low relative to v_P. This is generally the case because v_S increases with more rigid materials and with the degree of compaction, but v_S decreases only slightly with increasing saturation relative to dry sediments (Nur, 1982; Zhu and others, 2000).

Poisson's ratio (μ) can also be used to differentiate between sediments and crystalline rocks and between saturated and unsaturated sediments. Although μ can range from negative values to 0.5 (fluids = 0.5), μ for competent crystalline rocks is typically 0.25–0.3. For saturated sediments, in contrast, μ can be as high as ~0.495. The minimum μ for water-saturated sediments is ~0.43 (Catchings and others, 2006, 2014) to ~0.45 (Bowles, 1982; Pasquet and others, 2015), and the maximum μ for unsaturated sediments is generally less than 0.4. Lithological variations may account for observed μ variations in saturated materials in the shallow subsurface (Stuempel and others, 1984; Catchings and Lee, 1996; Salem, 2000; Uyanik, 2011), but for this study, we consider μ greater than 0.43 to indicate subsurface saturated sediments or partly saturated, clay-rich materials.

P-wave reflection imaging can be useful in identifying the top of groundwater, which forms an impedance contrast due to the sudden increase in v_P at the saturated/unsaturated interface within sediments. This increase in v_P can result in a strong reflection from the top of groundwater. Reflection imaging can also help differentiate basement from sediments because competent crystalline rocks (such as granitic rocks) are typically less reflective than layered sediments. However, the weathering zone near the top of crystalline rocks can form impedance contrasts that are seen as reflections from within the weathered crystalline rocks on reflection images. At Edwards AFB, water-well data show that such a weathered zone exists near the top of crystalline basement (Cromwell and Fenton, 2020; Earth Tech, Inc, 2006).

Fault Identification

Seismic methods can be particularly useful in identifying subsurface faults. Abrupt changes in v_P and v_S across faults, abrupt changes in the depth of the top of groundwater (v_P of 1,500 m/s), near-vertical zones of low v_P and v_S, near-vertical zones of high v_P/v_S ratios and μ, and offset reflectors are consistent with prominent zones of near-vertical faulting (Catchings and others, 2013, 2014, 2020). Any one of these observations on seismic images is consistent with faulting, but co-located areas of high v_P/v_S ratios, high μ, near-vertical zones of low v_S (and low v_P when surrounding rocks have v_P greater than ~2,500 m/s), offset reflectors, and diffractions provide a high degree of confidence in the existence of faulting at a specific location.

Seismic Data Acquisition

In June 2020, we acquired high-resolution P-wave seismic data along an ~3,000-m-long, northeast-southwest-trending profile in the northeastern part of Edwards AFB (fig. 1). The data were recorded using 400 three-component SmartSolo nodal seismometers (5 hertz) spaced at 5-m intervals, resulting in 600 recording sites along the linear profile. Each recording site included a corresponding co-located (1 m perpendicular offset) seismic shot point (source), resulting in 600 shot points along the seismic profile. At each shot point, the seismic sources were generated by a 227-kilogram accelerated weight drop (AWD) used to

vertically strike an aluminum plate on the ground surface. We also used small explosions (0.151 kilograms) detonated about 2 meters (m) below the ground surface at every 20th shot point. The more powerful explosive shots generated better propagation, and they allowed us to use reciprocal arrivals when arrivals from the AWD shots were less clear.

We acquired the data using active seismometers on both sides of each shot point (except at the end points), which allowed for reversing ray paths along the seismic profile. For the initial deployment, 400 seismometers, spaced at 5-m intervals, were deployed along the southwestern ~2,000 m of the seismic profile. AWD seismic sources were generated along the first 300 shot points (spanning 1,500 m) and recorded by the stationary array. In addition, explosive shots were generated every 100 m along the entire ~3,000-m-long profile. The 200 southwesternmost channels of the array were then moved to the northeastern part of the seismic profile, leaving 100 active channels (spanning ~500 m) southwest of the original northeasternmost shot point and 300 active channels (spanning ~1,500 m) northeast of that shot point. AWD seismic sources were then generated along the remainder of the seismic profile, and explosive shots were repeated every 100 m along the entire 3,000-m-long profile. There was a total of ~240,000 seismic traces that could be analyzed in generating the tomographic velocity models. These data are available in an associated data release by Goldman and others (2021).

Each seismic source (shot) generated at the 600 shot points was recorded by 400 seismometers, allowing for high redundancy. Because seismic sources were dominantly compressional (explosions and vertical weight drops), the recorded data are dominantly compressional body waves and their associated surface (Rayleigh) waves. Timing and locations were determined using Global Positioning System (GPS) data. The nodal seismometers record a GPS time and three-dimensional location every 6 seconds, and because the arrays recorded continuously for several days, more than 25,000 GPS locations were determined by averaging, resulting in centimeter-scale accuracy. These data showed that topography varies by approximately 25 m over the ~3,000-m-long profile.

Seismic Data and Data Processing

Example explosive shot gathers from the southwestern, central, and northeastern parts of the seismic profile are shown in figure parts 2*A*, 2*B*, and 2*C*, respectively. The seismic energy propagated well along the seismic profile, resulting in clear first arrivals from most shot points. However, one area of the profile has an apparent subsurface structure that channeled seismic P-wave energy at about 1,400 m/s. Although this channeled energy did not affect the first arrivals or the tomography images, it was necessary to surgically remove that energy prior to developing reflection images. We believe this structure is likely manmade and near the surface, although Edwards AFB personnel stated they are unaware of a manmade structure in that area.

The data acquisition geometry allowed us to develop multiple types of seismic models and images, including high-resolution P-wave refraction tomography velocity models (v_P models), an S-wave MASW velocity model (v_S model), a v_P/v_S ratio model, a μ model, P-wave reflection images, and combinations of all images.

Our refraction tomography models were developed using the tomography code of Hole (1992), and the reflection data were processed using ProMax, a commercial interactive data processing package. We developed the v_S model from Rayleigh waves (recorded on the P-wave data set, see figure 2) using a version of the MASW method provided in the Geometrics 2D software package described in Hayashi and Suzuki (2004) and Hayashi (2008). We refer to the v_S model presented in this report as the MASW v_S velocity model. We combined our P-wave tomography model (v_P model) with our MASW v_S model to develop models of v_P/v_S ratios and μ values. However, the MASW method produces a series of one-dimensional (1D) models that are merged to form a two-dimensional (2D) model. As such, large, abrupt topographic variations can result in slight velocity-depth inaccuracies, although few such topographic variations exist along the seismic profile.

P-Wave Refraction Tomography Velocity Model

Using the code of Hole (1992), we developed v_P models from first-arrival refractions measured on P-wave shot gathers (fig. 2). The algorithm uses finite differences (solving the eikonal equation) to compute first-arrival travel times from the source to the receiver in a starting velocity model, which was developed from 1D analysis of the shot gathers along the profile. The algorithm then uses back-projection of the data misfits to update the model. This process is repeated in iterative steps until a satisfactory fit is obtained among observed and calculated first arrivals, resulting in a final model. We used multiple starting models, and all final models were similar, with less than ~5 percent variation among the final models where best resolved.

We initially developed a 2D v_P model using a 5-m by 5-m grid spacing and as many as 240,000 first arrivals, which allow for a high degree of redundancy and high resolution within the velocity model (fig. 3). Using the full range of offsets between the shots and receivers allowed for us to develop a maximum-depth (~400 m) v_P model that focuses on the large-scale features of the shallow crust, but the shallow structure is slightly less resolved. To achieve higher resolution at shallow depths, we also inverted first arrivals for a 2D model using a 3-m by 3-m grid spacing and a subset of the first arrivals that were closer (within 600 m) to

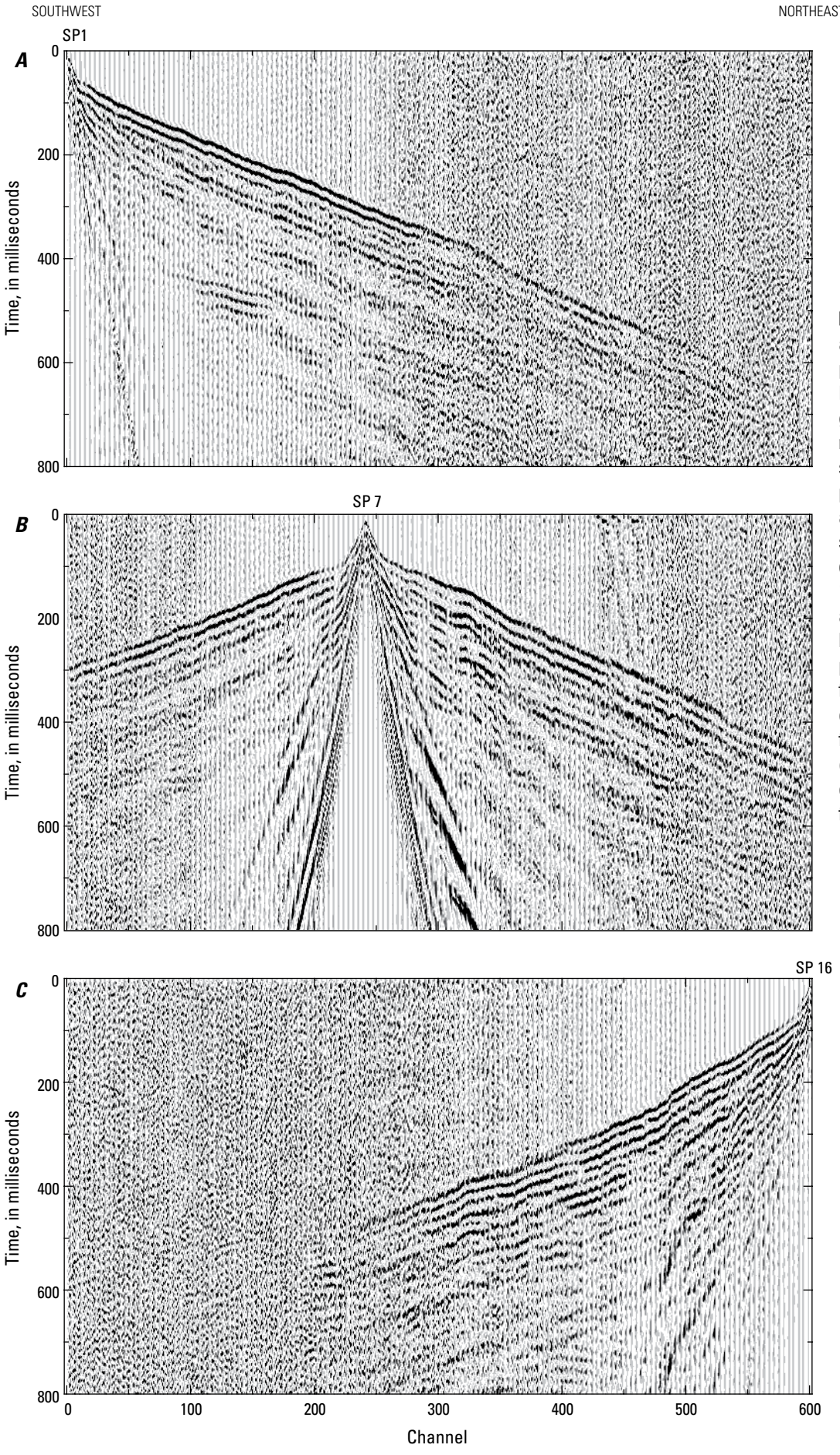

Figure 2. Example shot gathers along the Edwards seismic profile, Edwards Air Force Base, California. The data were generated at shot points located near the southwest end of the seismic profile (*A*), the central part of the seismic profile (*B*), and the northeast end of the seismic profile (*C*). A shallow-depth feature between channels 100 and 325 generated an anomalous wave that reflected back and forth between its end points. This wave can be seen for all shot points between the end points. Example shot gathers from the southwest end (*D*), central part (*E*), and northeast end (*F*) of the shallow-depth feature are shown.

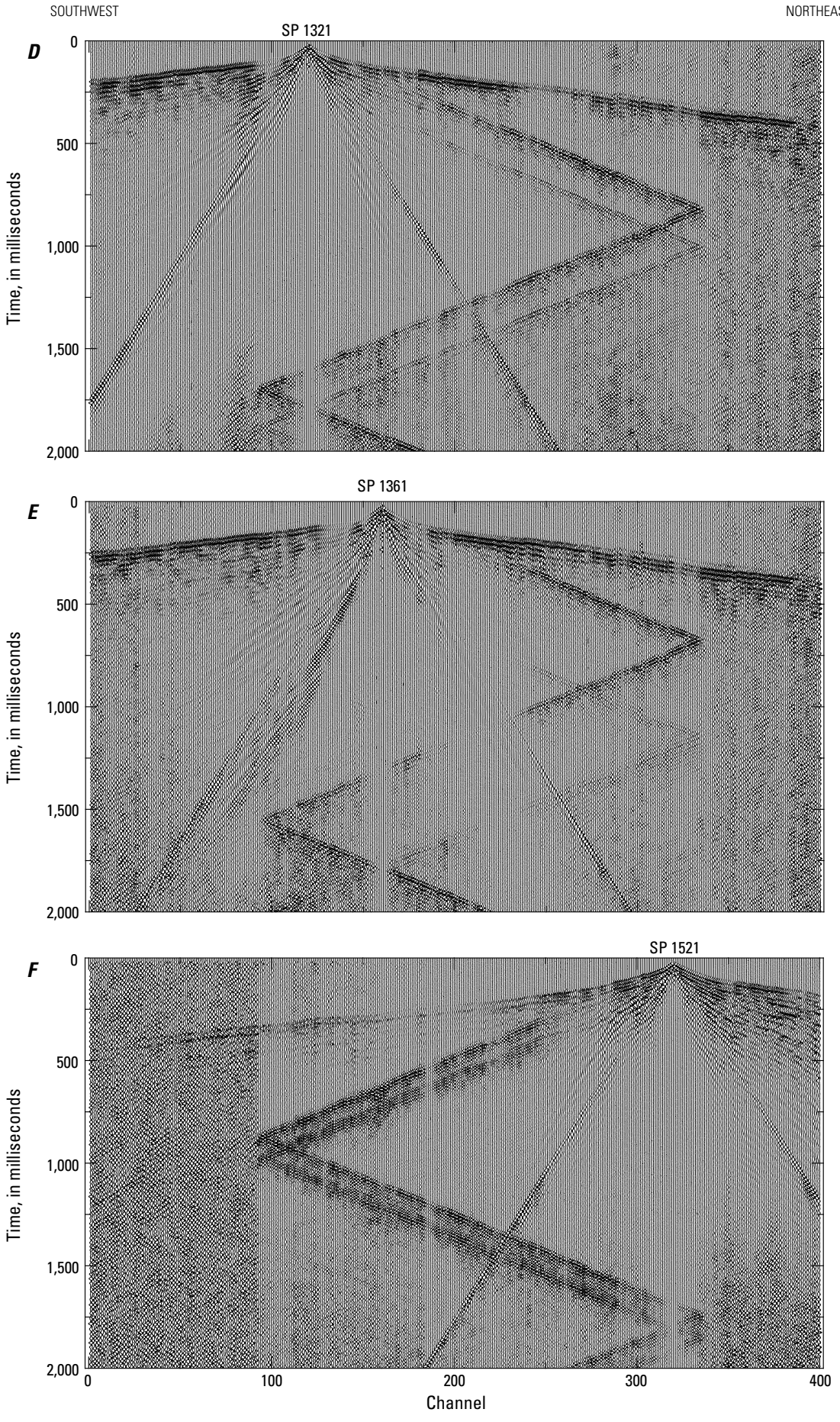

Figure 2.—Continued Example shot gathers along the Edwards seismic profile, Edwards Air Force Base, California. The data were generated at shot points located near the southwest end of the seismic profile (*A*), the central part of the seismic profile (*B*), and the northeast end of the seismic profile (*C*). A shallow-depth feature between channels 100 and 325 generated an anomalous wave that reflected back and forth between its end points. This wave can be seen for all shot points between the end points. Example shot gathers from the southwest end (*D*), central part (*E*), and northeast end (*F*) of the shallow-depth feature are shown.

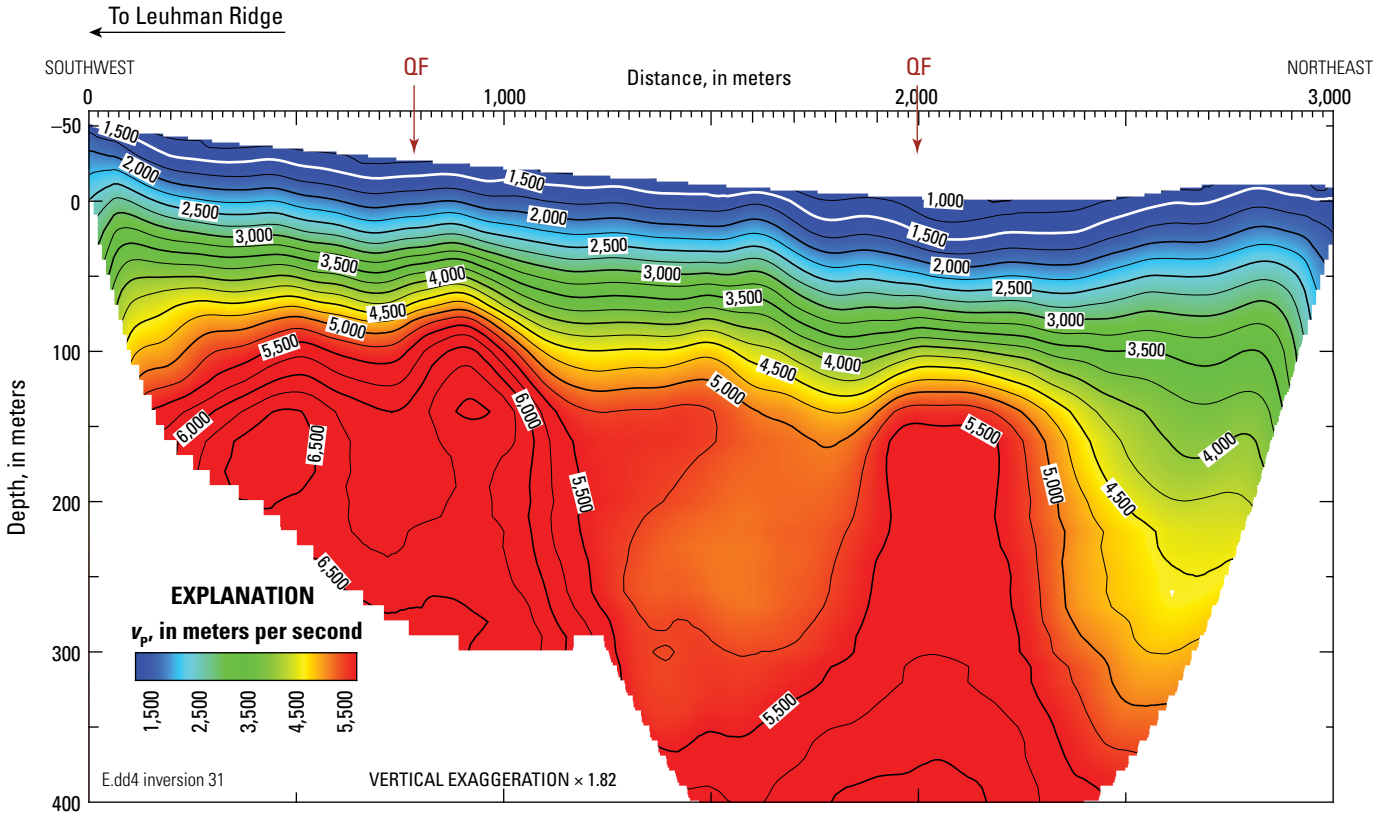

Figure 3. Two-dimensional compressional-wave velocity (v_P) tomography model along the Edwards seismic profile (Edwards Air Force Base, California), generated using first arrivals (as many as 240,000) and a node spacing of 5 meters. Prominent near-vertical, low-velocity zones occur at several locations along the seismic profile. Locations of inferred Quaternary faults (Bryant, 2017) shown in figure 2 are labeled QF. The southwestern and northeastern QFs are referred to as the Leuhman and Spring Faults, respectively, by Bryant (2017). Contours show v_P in meters per second (m/s). The white line highlights the 1,500-m/s v_P contour, which generally correlates with the top of groundwater.

each shot point (fig. 4). The shorter offsets between the shots and the receivers resulted in a shallower maximum-depth (~200 m) v_P model that has higher resolution in the shallow subsurface. These models show that v_P ranges from ~1,000 m/s near the surface to ~6,000 m/s at about 400 m depth (fig. 3).

Multichannel Analysis of Surface Waves (MASW) Shear-Wave (S-Wave) Velocity Modeling

We developed a v_S model (fig. 5) from surface (Rayleigh) waves that were recorded on our P-wave shot gathers of the Edwards seismic profile (fig. 2). We used a total of 16 explosive shot gathers and 601 receivers to construct 150 common midpoint cross-correlation gathers from 899 common midpoints. Thus, a gather was evaluated every 20 m along the profile, and the 2D v_S model was derived from 150 dispersion curves. The derived v_S model is averaged over greater distances (20 m) than the v_P model (5 m) and provides less resolution. Our v_S model shows that v_S ranges from about 500 m/s near the surface to 4,000 m/s in the upper ~400 m along the profile.

Model of the Ratio of Compressional-Wave Velocity to Shear-Wave Velocity (v_P/v_S Ratio)

We developed a model of the ratio of compressional-wave velocity to shear-wave velocity (v_P/v_S ratio) along the seismic profile (fig. 6) using the method of Catchings and others (2020). The v_P and v_S models were parametrized with the same grid spacings (3 m by 3 m), allowing a v_P/v_S ratio to be calculated at each grid point of the models. However, the maximum depth of imaging was shallower for the higher-resolution v_P model (3-m by 3-m grid spacing) (fig. 4) than for the MASW v_S model (fig. 5), so the v_P/v_S ratio model extends only to the maximum depth of the high-resolution v_P model (~200 m). In addition, because of the lower resolution of the v_S model, the v_P/v_S ratio model is necessarily averaged over longer lateral and vertical distances than the v_P model. As a result, anomalies in the v_P/v_S ratio model can be spread over slightly greater lateral and vertical distances. The v_P/v_S ratios in the model range from about 1.5 to greater than 3.25, with the lowest ratios predominantly in the deeper rocks, which are likely granitic basement.

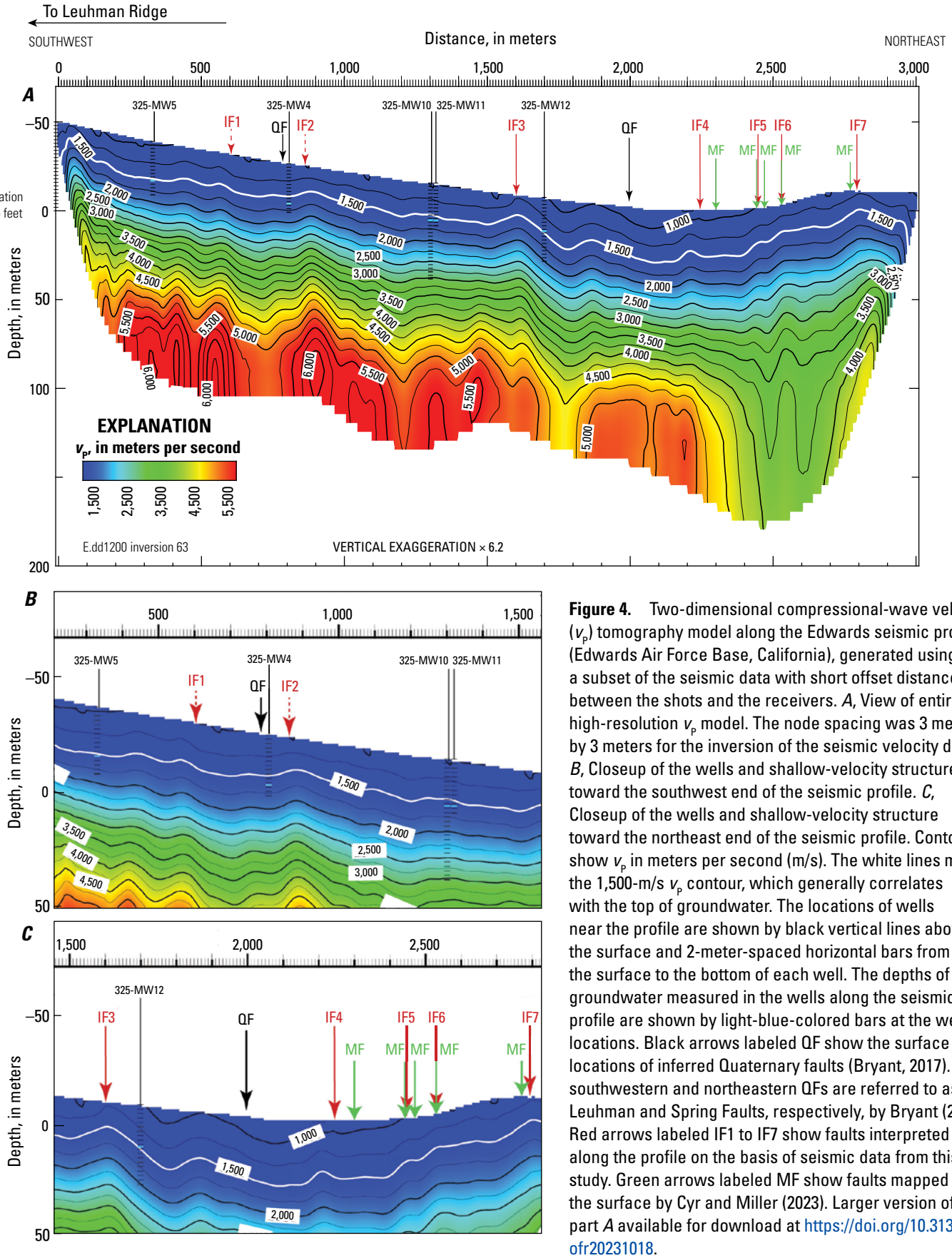

Figure 4. Two-dimensional compressional-wave velocity (v_P) tomography model along the Edwards seismic profile (Edwards Air Force Base, California), generated using a subset of the seismic data with short offset distances between the shots and the receivers. *A*, View of entire high-resolution v_P model. The node spacing was 3 meters by 3 meters for the inversion of the seismic velocity data. *B*, Closeup of the wells and shallow-velocity structure toward the southwest end of the seismic profile. *C*, Closeup of the wells and shallow-velocity structure toward the northeast end of the seismic profile. Contours show v_P in meters per second (m/s). The white lines mark the 1,500-m/s v_P contour, which generally correlates with the top of groundwater. The locations of wells near the profile are shown by black vertical lines above the surface and 2-meter-spaced horizontal bars from the surface to the bottom of each well. The depths of groundwater measured in the wells along the seismic profile are shown by light-blue-colored bars at the well locations. Black arrows labeled QF show the surface locations of inferred Quaternary faults (Bryant, 2017). The southwestern and northeastern QFs are referred to as the Leuhman and Spring Faults, respectively, by Bryant (2017). Red arrows labeled IF1 to IF7 show faults interpreted along the profile on the basis of seismic data from this study. Green arrows labeled MF show faults mapped at the surface by Cyr and Miller (2023). Larger version of part *A* available for download at https://doi.org/10.3133/ofr20231018.

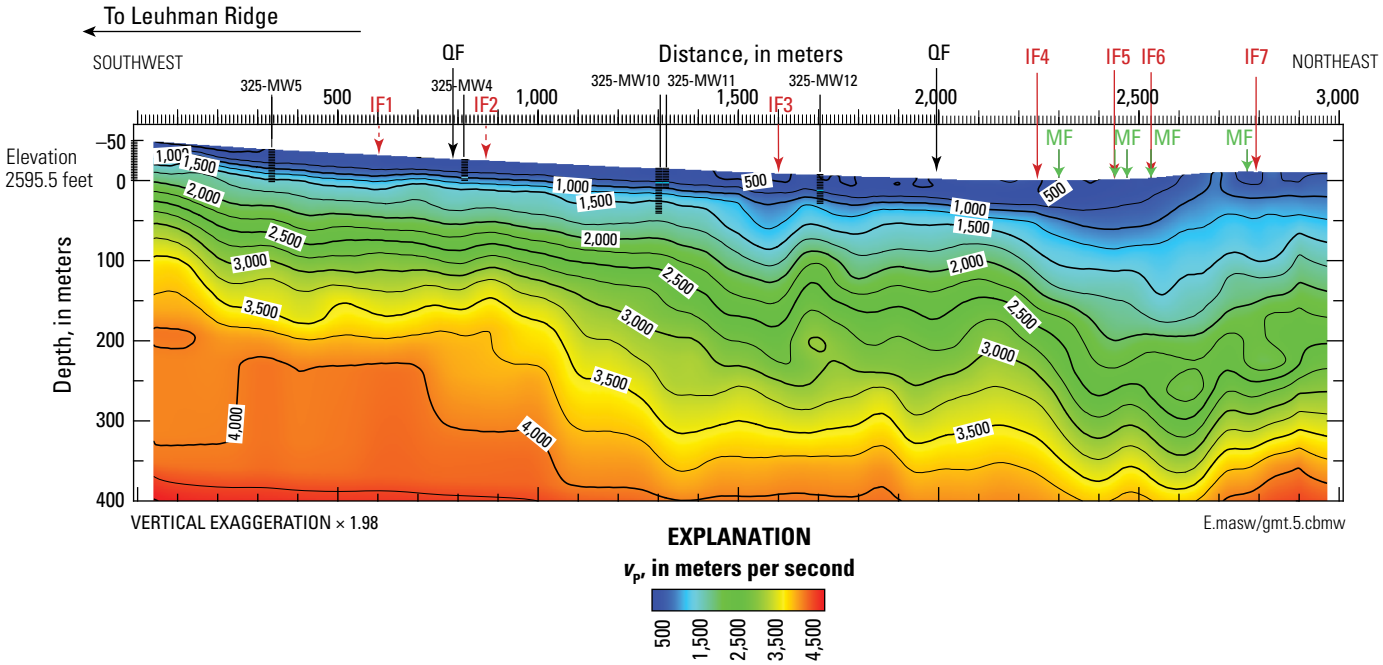

Figure 5. Two-dimensional shear-wave velocity model along the Edwards seismic profile (Edwards Air Force Base, California) developed from Rayleigh surface waves and the multichannel analysis of surface waves modeling technique. Contours show shear-wave velocity (v_p) in meters per second (m/s). The locations of wells near the profile are shown with black vertical lines above the surface and 2-meter-spaced horizontal bars from the surface to the bottom of each well. The depths of groundwater measured in the wells along the seismic profile are shown by light-blue-colored bars at the well locations. Black arrows labeled QF show the surface locations of inferred Quaternary faults (Bryant, 2017). The southwestern and northeastern QFs are referred to as the Leuhman and Spring Faults, respectively, by Bryant (2017). Red arrows labeled IF1 to IF7 show faults interpreted along the profile on the basis of seismic data from this study. Green arrows labeled MF show faults mapped at the surface by Cyr and Miller (2023). Larger version of figure available for download at https://doi.org/10.3133/ofr20231018.

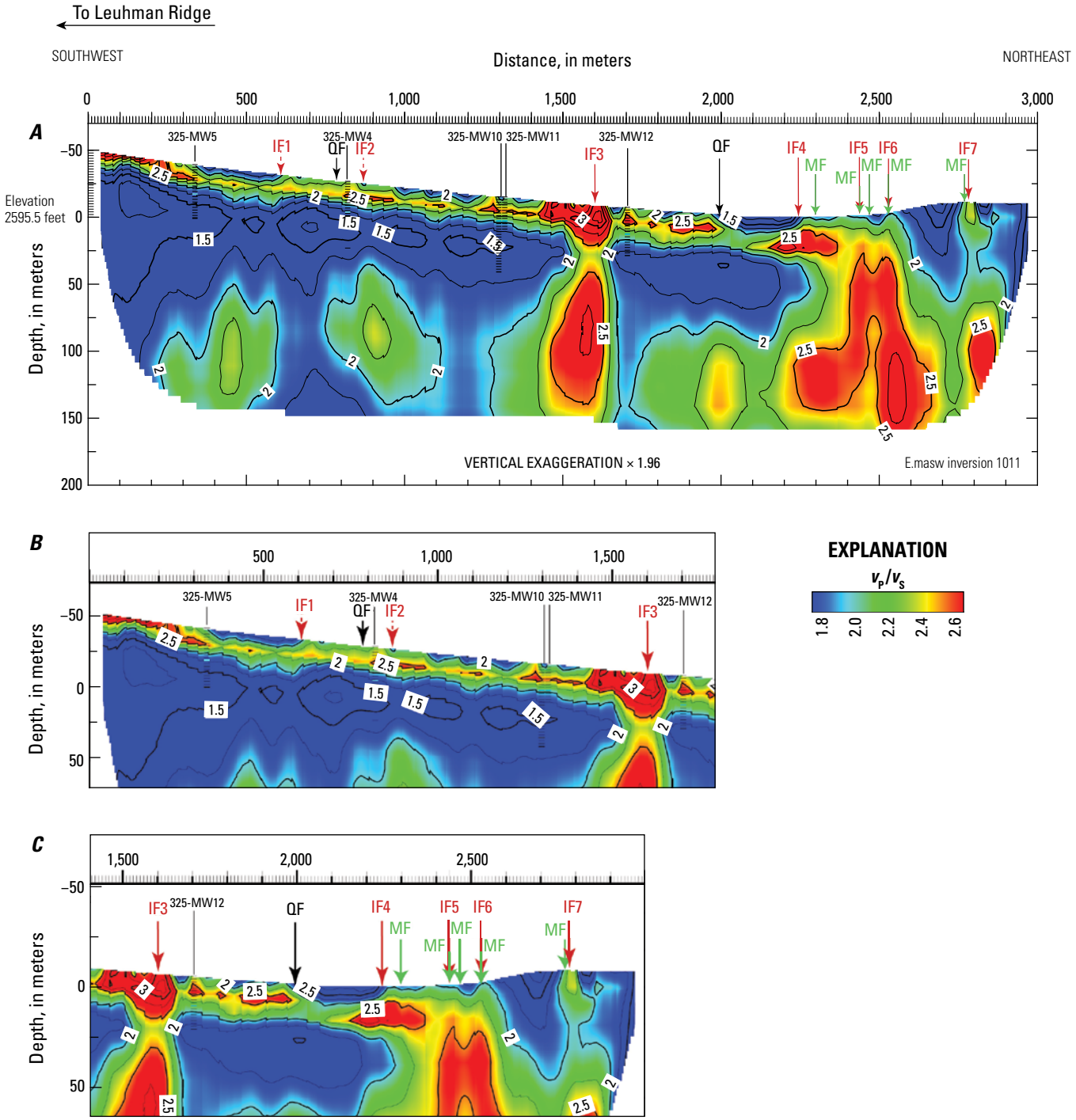

Figure 6. Two-dimensional model of the ratio of compressional-wave velocity to shear-wave velocity (v_P/v_S ratio) along the Edwards seismic profile (Edwards Air Force Base, California), derived from the tomographic compressional-wave velocity (v_P) model and the multichannel analysis of surface waves (MASW) shear-wave velocity (v_S) model. *A*, Full extent of model. *B*, Closeup view of shallow southwestern part of model. *C*, Closeup view of shallow northeastern part of model. Contours show v_P/v_S ratios. The locations of wells near the profile are shown with black vertical lines above the surface and 2-meter-spaced horizontal bars from the surface to the bottom of each well. The depths of groundwater measured in the wells along the seismic profile are shown by light-blue-colored bars at the well locations. Black arrows labeled QF show the surface locations of inferred Quaternary faults (Bryant, 2017). The southwestern and northeastern QFs are referred to as the Leuhman and Spring Faults, respectively, by Bryant (2017). Red arrows labeled IF1 to IF7 show faults interpreted along the profile on the basis of seismic data from this study. Green arrows labeled MF show faults mapped at the surface by Cyr and Miller (unpub. data, 2020). Larger version of part *A* available for download at https://doi.org/10.3133/ofr20231018.

Poisson's Ratio (μ) Model

We also used the v_P and v_S models to develop a model of μ along the seismic profile (fig. 7) on the basis of the relationship of Thomsen (1990):

$$\mu = \frac{v_P^2 - 2v_S^2}{2(v_P^2 - v_S^2)} . \quad (1)$$

Because of the lower resolution of the v_S model, the μ model has lower resolution than the v_P model. Our μ model shows relatively high values at shallow depths along much of the seismic profile, with minimum values of about 0.10 and maximum values greater than 0.45.

Seismic Reflection Image

We developed a seismic reflection (stack) image along the Edwards seismic profile (fig. 8*A*, *B*) using P-wave waveforms from the seismic data and the tomographic v_P model shown in figure 4. Processing steps included geometry installation, independent trace editing, timing corrections, elevation static corrections, automatic gain control (AGC), bandpass filtering, surgical muting, velocity analysis (from refractions), normal moveout (NMO) correction, stretch muting, common depth point (CDP) stacking, post-stack, post-stack bandpass filtering, and post-stack deconvolution. For velocities at depths greater than those of the tomography velocity model, we used 1D velocity estimates from reflection parabolas on shot gathers, and we inferred velocities on the basis of laboratory-determined velocity-depth (pressure) relations (Carmichael, 1989). Because of the 5-m shot and geophone spacing, the seismic reflection images have a common depth point spacing of 2.5 m along the entire 3,000-m-long profile, thereby providing very high spatial resolution.

Combined Velocity and Reflection Images

To better understand lithologic and structural variations along the seismic profile, we superimposed our velocity-related images on the reflection image. Figure parts 8*C*, 8*D*, 8*E*, and 8*F* show the superimposed v_P, v_S, v_P/v_S ratio, and μ models, respectively. These images allow direct comparison between the velocity-related models, which measure various aspects of the subsurface, and the reflection image.

Interpretations

Our seismic images show that the shallow subsurface in northeastern Edwards AFB is geologically and tectonically complex, with significant lateral and vertical variations in structure and lithology. Comparing the seismic images (velocities, velocity ratios, and reflection) with surface geology and borehole information helps constrain the shallow stratigraphy, lithology, groundwater depth variations, and faulting in northeastern Edwards AFB.

Lithology-Velocity Correlations

Because of differences in mineral composition, water saturation, faulting, fracturing, and compaction (based on depth of burial), seismic velocities are not unique to specific rocks. Generally, however, subsurface material classes can be inferred from seismic velocity data. Examples of such classes include unconsolidated versus consolidated sediments, saturated versus unsaturated materials, sediments versus crystalline rocks, and weathered versus unweathered rocks. Weathering also has a large effect on seismic velocity in most near-surface locations. Combined, these principles allow us to infer rock types along the Edwards seismic profile on the basis of velocities and weathering (table 1).

At Edwards AFB, well logs indicate that boundaries between various subsurface materials are gradational and vary in depth and composition laterally; thus, it is difficult to precisely identify boundaries from seismic velocity measurements alone or to extrapolate boundaries laterally between wells. We can, however, infer likely lithologies and physical conditions on the basis of other empirical studies.

In a study with similar methodology to this one, Olona and others (2010) used a combination of seismic refraction v_P, MASW v_S, other seismic measurements, borehole lithology, and resistivity to infer rock classifications for rocks in a calc-alkaline monzogranite massif (informally referred to as the Carlés granite massif) in northwest Spain. They correlated v_P and v_S with weathering profiles, as shown in table 2. However, large topographic variations along their seismic profiles may have significantly affected their estimates of MASW-derived v_S.

Table 1. International Society of Rock Mechanics weathering classification (Brown, 1981).

Class	Term	Description
I	Fresh rock	No visible sign of rock material weathering
II	Slightly weathered rock	Discoloration indicates weathering of rock materials and discontinuity surfaces
III	Moderately weathered rock	Less than half of the rock material is decomposed and/or disintegrated to soil
IV	Highly weathered rock	More than half of the rock material is discomposed and/or disintegrated to soil
V	Completely weathered rock	All rock material is decomposed and/or disintegrated to soil. The original mass structure is still largely intact
VI	Residual soil	All rock material is converted to soil. The mass structure and material fabric are destroyed

Table 2. Lithology classification based on seismic velocity in northwest Spain (from Olona and others, 2010).

[v_P, compressional-wave velocity; v_S, shear-wave velocity; m/s, meters per second; N/A, not available]

Type	Description	Weathering grade	v_P, in m/s	v_S, in m/s
1	Sandy soil (granite source)	V–VI	600–1,000	230–297
2	Soil (fully or partially weathered from granite)	II–IV	1,400–1,450	275–528
3	Fresh rock (granite)	I–II	2,600–3,100	600–1,166
4	Fresh rock (granite)	I–II	4,100–5,500	N/A

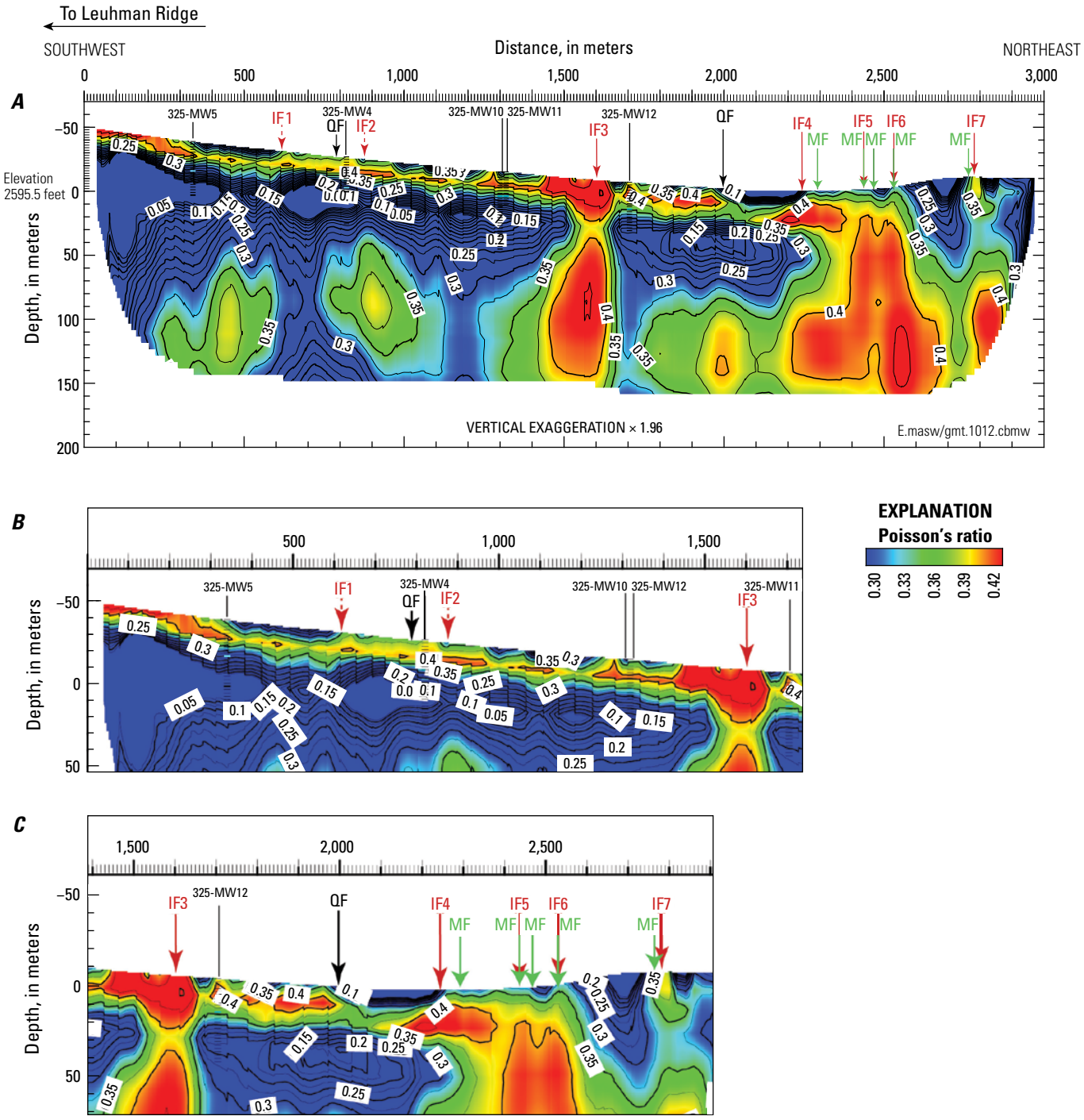

Figure 7. Two-dimensional Poisson's ratio (μ) model along the Edwards seismic profile (Edwards Air Force Base, California), derived from the tomographic compressional-wave velocity (v_p) model and the multichannel analysis of surface waves shear-wave velocity (v_s) model. *A*, Full extent of model. *B*, Closeup view of shallow southwestern part of model. *C*, Closeup view of shallow northeastern part of model. Contours show μ. The locations of wells near the profile are shown with black vertical lines above the surface and 2-meter-spaced horizontal bars from the surface to the bottom of each well. The depths of groundwater measured in the wells along the seismic profile are shown by light-blue-colored bars at the well locations. Black arrows labeled QF show the surface locations of inferred Quaternary faults (Bryant, 2017). The southwestern and northeastern QFs are referred to as the Leuhman and Spring Faults, respectively, by Bryant (2017). Red arrows labeled IF1 to IF7 show faults interpreted along the profile on the basis of seismic data from this study. Green arrows labeled MF show faults mapped at the surface by Cyr and Miller (2023). Larger version of part *A* available for download at https://doi.org/10.3133/ofr20231018.

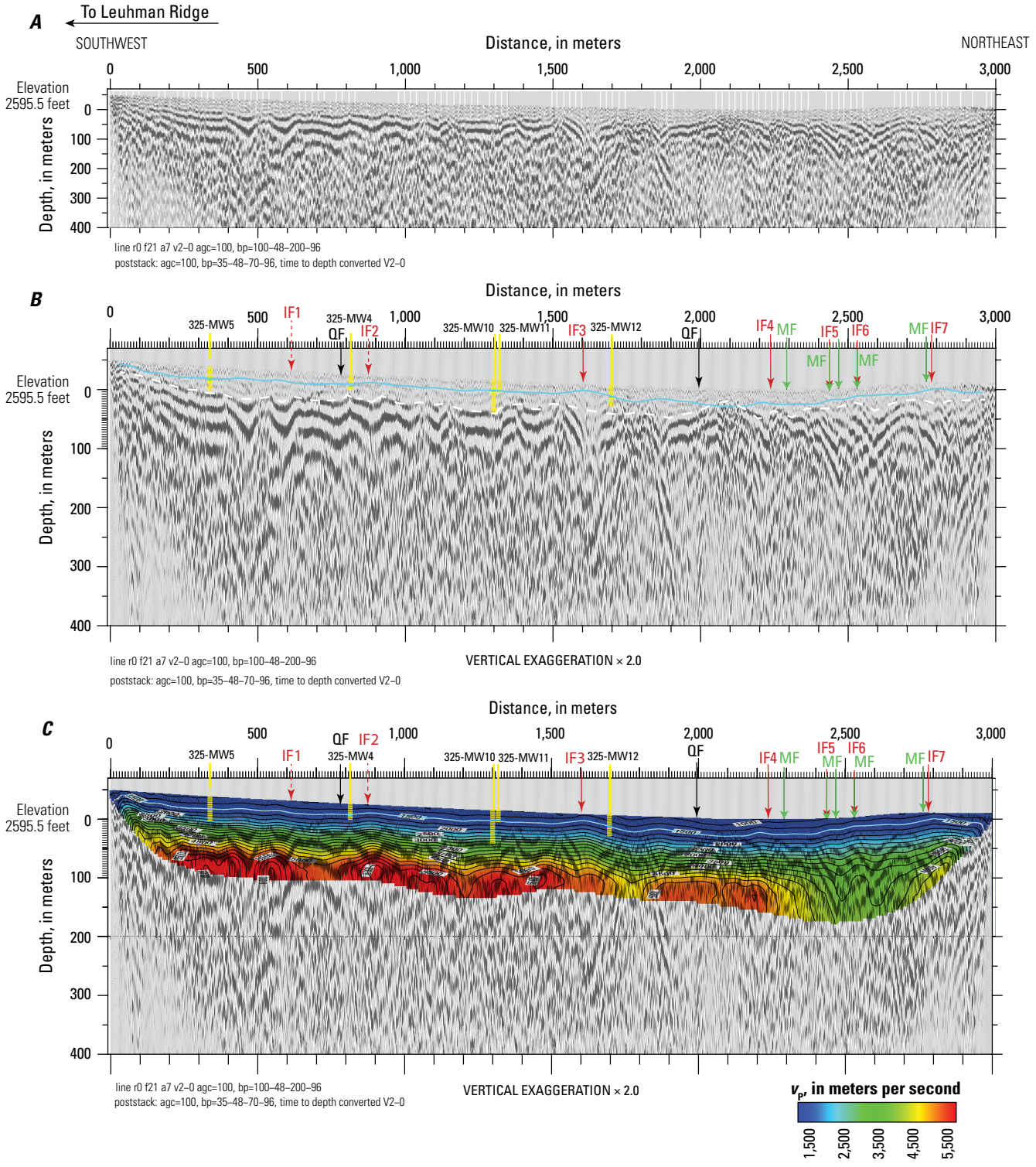

Figure 8. Unmigrated reflection image of the upper 400 meters (depth) along the Edwards seismic profile, Edwards Air Force Base, California. *A*, Unmigrated reflection image of the upper 400 meters without annotations. Elevation is relative to the topographically lowest point along the profile. Strong diffractions (inverted V-shaped reflections) exist at multiple locations along the seismic profile. *B*, Vertically exaggerated (× 2) unmigrated reflection image from part *A*. *C*, Reflection image from part *B* superimposed on the compressional-wave velocity (v_P) tomography model (fig. 4*A*). *D*, Reflection image from part *B* superimposed on the shear-wave velocity (v_S) model (fig. 5). *E*, Reflection image from part *B* superimposed on the ratio of compressional-wave velocity to shear-wave velocity (v_P/v_S ratio) model (fig. 6). *F*, Reflection image from part *B* superimposed on the Poisson's ratio (μ) model (fig. 7). Annotations show the locations of wells adjacent to the seismic profile (yellow), the depth to groundwater as indicated by the 1,500-m/s compressional-wave velocity (v_P) contour (light blue line), the top of weathered basement rocks (dashed white line), inferred Quaternary faults from Bryant (2017) (black arrows labeled QF), recently mapped faults from Cyr and Miller (2023) (green arrows labeled MF), and interpreted faults from this study (red arrows labeled IF1 to IF7). The southwestern and northeastern QFs are referred to as the Leuhman and Spring Faults, respectively, by Bryant (2017). Larger version of figure available for download at https://doi.org/10.3133/ofr20231018.

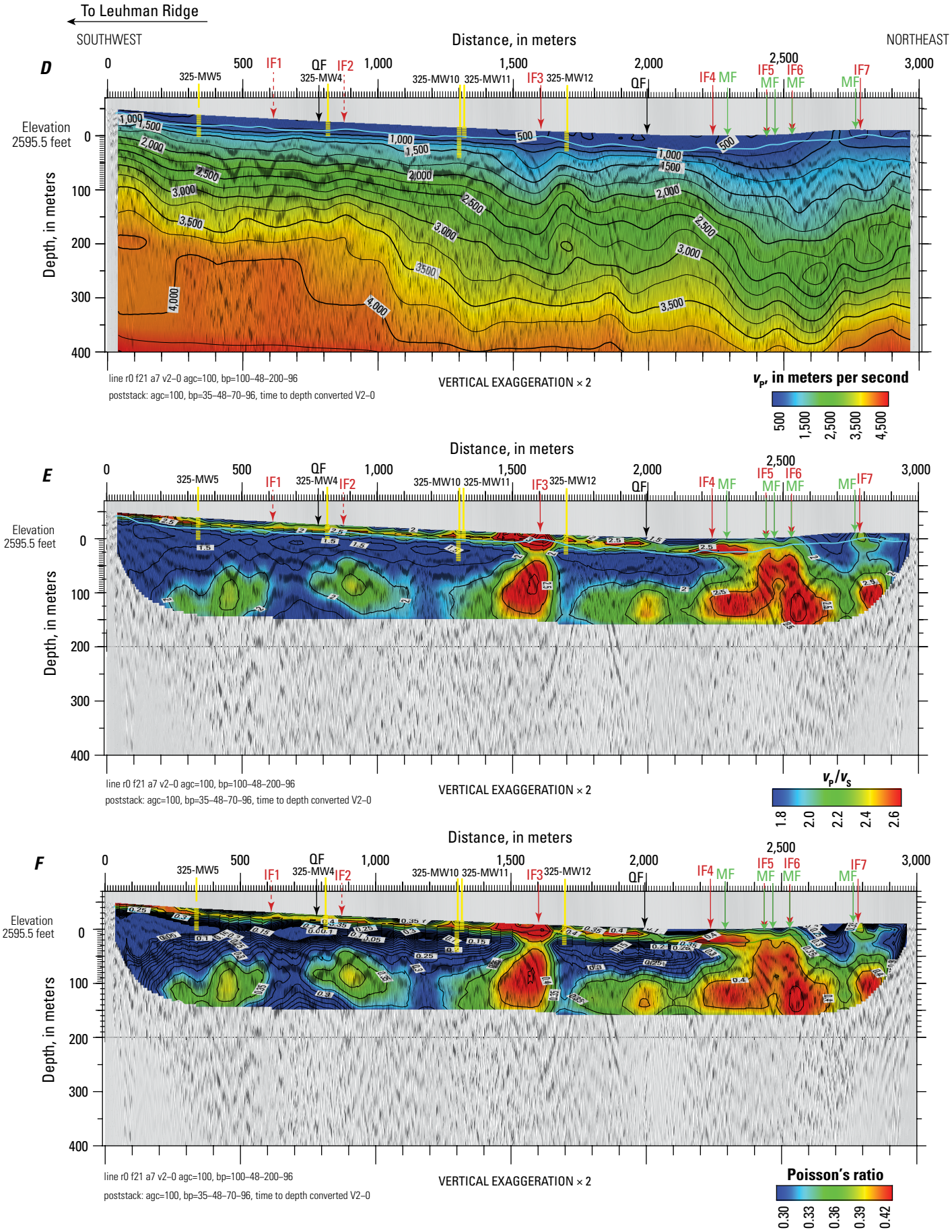
To Leuhman Ridge
SOUTHWEST
NORTHEAST
D
E
F
Distance, in meters
Elevation 2595.5 feet
Depth, in meters
325-MW5
325-MW4
325-MW10
325-MW11
325-MW12
IF1
IF2
IF3
IF4
IF5
IF6
IF7
QF
MF
VERTICAL EXAGGERATION × 2
line r0 f21 a7 v2–0 agc=100, bp=100–48–200–96
poststack: agc=100, bp=35–48–70–96, time to depth converted V2–0
v_P, in meters per second
v_P/v_S
Poisson's ratio

In another study of an area geographically closer to Edwards AFB, Zappe (1979) used downhole measurements (80–160 m depth) recorded in nine boreholes in the western and eastern Mojave Desert to determine v_P and v_S of largely unweathered granite; he determined v_P to be about 4,400 km/s and v_S to be ~1,700–2,700 km/s, with μ of 0.27–0.36. Zappe (1979) observed slightly lower velocities in the western Mojave Desert than in the eastern Mojave Desert, which he attributed to increased fracturing near the Garlock Fault Zone.

In a study of the Southern Sierra Critical Zone Observatory, located near Edwards AFB (to the northeast), Holbrook and others (2014) used refraction tomography studies to categorize saprolite as v_P <2 km/s, moderately weathered bedrock as v_P ~2 km/s to 4 km/s, and pristine granite as v_P >4 km/s. Although their study area did not have overlying sediments, the study still provides average velocities that are useful in inferring granitic rock types at Edwards AFB. Several other refraction tomography studies in the Mojave Desert and other places in California by Catchings and others (1999a, b, 2000, 2002) also provide insights into subsurface materials at Edwards AFB. Their sites included sediments overlying granites, and their studies included borehole observations and velocity measurements. Generally, they found that unconsolidated sediments (v_P <2,500 m/s), weathered granite rock (v_P of ~2,500–4,000 m/s), and fresh granite rock (v_P >4 km/s) have consistent velocity ranges in differing locations, but factors such as faulting and fracturing, depth of burial, and saturation can have large effects on those velocities.

These previous studies provide a general guide of expected velocities for granitic rocks in the Edwards AFB region. By combining velocity data with known lithology from boreholes at Edward AFB, we inferred the general composition, v_P velocities, v_S velocities, v_P/v_S ratios, and μ of lithologic classes along the profile, as shown in table 3. However, zones of intense faulting have been mapped along parts of the Edwards seismic profile (fig. 9); these can result in considerably lower seismic velocities, which in turn can strongly affect interpretations. As a result, we combine multiple forms of seismic data with borehole data (fig. 10) to interpret the lithology, structure, and physical conditions of the subsurface (figs. 11, 12) along the profile. Because one-dimensional velocity models for shallow granite rock may be useful to some researchers, we provide 1D models for every 500 m along the v_P and v_S models in appendix figures 1.1–1.3.

Table 3. Interpreted classification of subsurface lithology (outside of fault zones) at Edwards Air Force Base based on v_P, v_S, v_P/v_S ratios, μ, and reflection data.

[v_P, compressional-wave velocity; v_S, shear-wave velocity; v_P/v_S ratio, ratio of compressional-wave velocity to shear-wave velocity; μ, Poisson's ratio; m/s, meters per second]

Type	Description	Weathering grade	v_P, in m/s	v_S, in m/s	v_P/v_S ratio	μ
1	Sandy soil, gravel, etc. (unsaturated)	V–VI	1,000–1,500	500–750	1.5–2.5	0.35–0.40
2	Soil (saturated, fully or partially weathered from granite)	III–IV	1,500–2,500	750–1,500	1.5–2.0	0.1–0.35
3	Weathered or fractured granite rock (granite)	III	2,500–4,000	1,500–2,700	1.5–2.0	0.15–0.25
4	Fresh granite rock (unfractured or fractured and saturated)	I–II	4,000–6,000	>2,700	1.5–2.0	0.25–0.30

Figure 9. Annotated satellite image of the area around the Edwards seismic profile at Edwards Air Force Base, California. Mapped faults (red lines) are by Cyr and Miller (2023) and inferred Quaternary faults (yellow lines) are from the U.S. Geological Survey Quaternary Fault and Fold Database (Bryant, 2017). Seismometer locations are shown as light-blue-colored circles. Water-well locations along the seismic profile are shown as black circles.

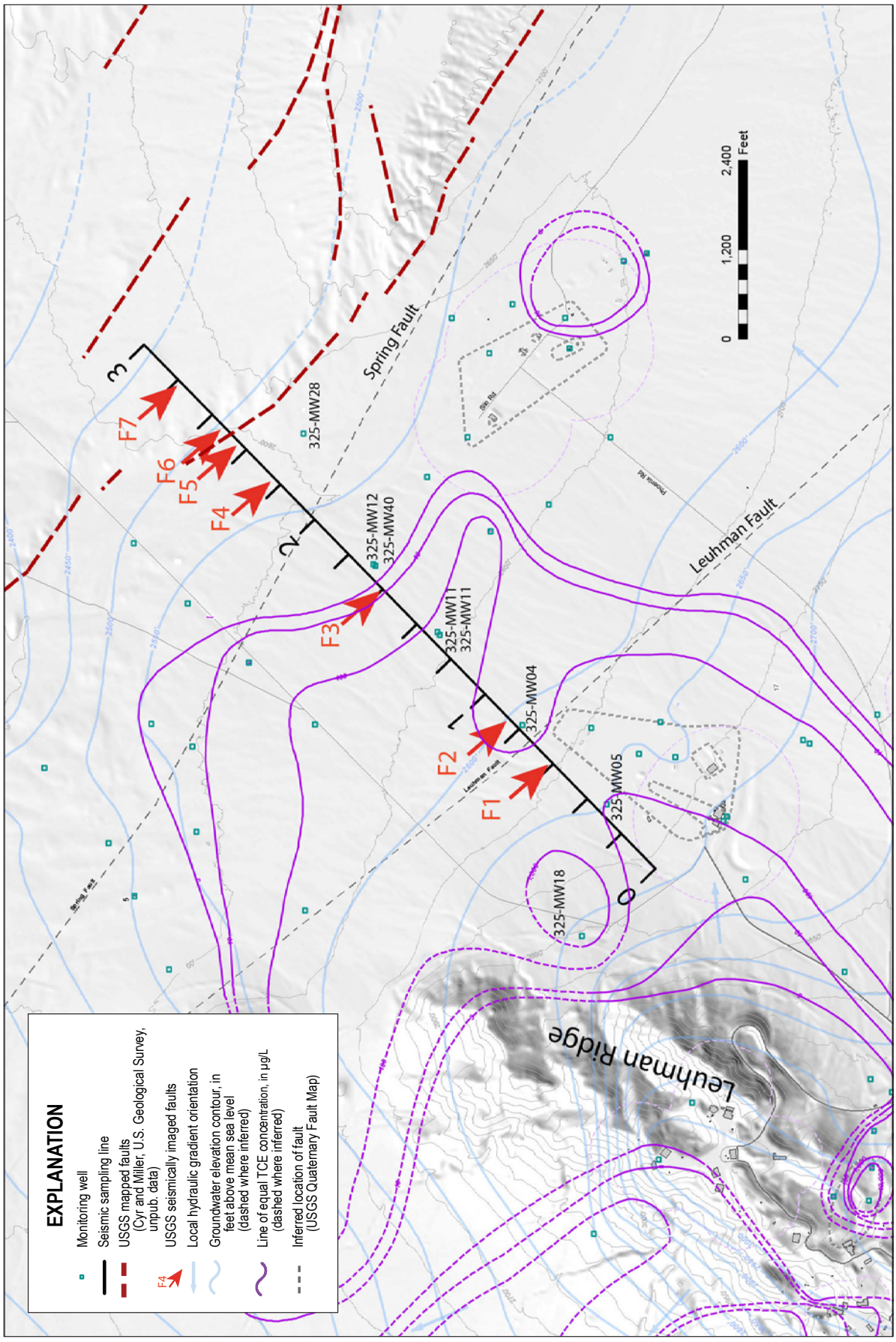

Figure 10. Isocontour map of Trichloroethylene (TCE) contaminants, as reported by the U.S. Air Force at Edwards Air Force Base, California, in 2020 (U.S. Air Force, 2022), featuring the area around the Edwards seismic profile (solid black line with numbers). Other major features on the map include hydraulic gradient orientation, groundwater elevation contours, well locations, and mapped faults. The numbers on the seismic profile refer to distance in kilometers from the southwest to the northeast ends. Red arrows labeled F1 to F7 along the profile show the locations of seismically interpreted faults. USGS, U.S. Geological Survey; µg/L, micrograms per liter.

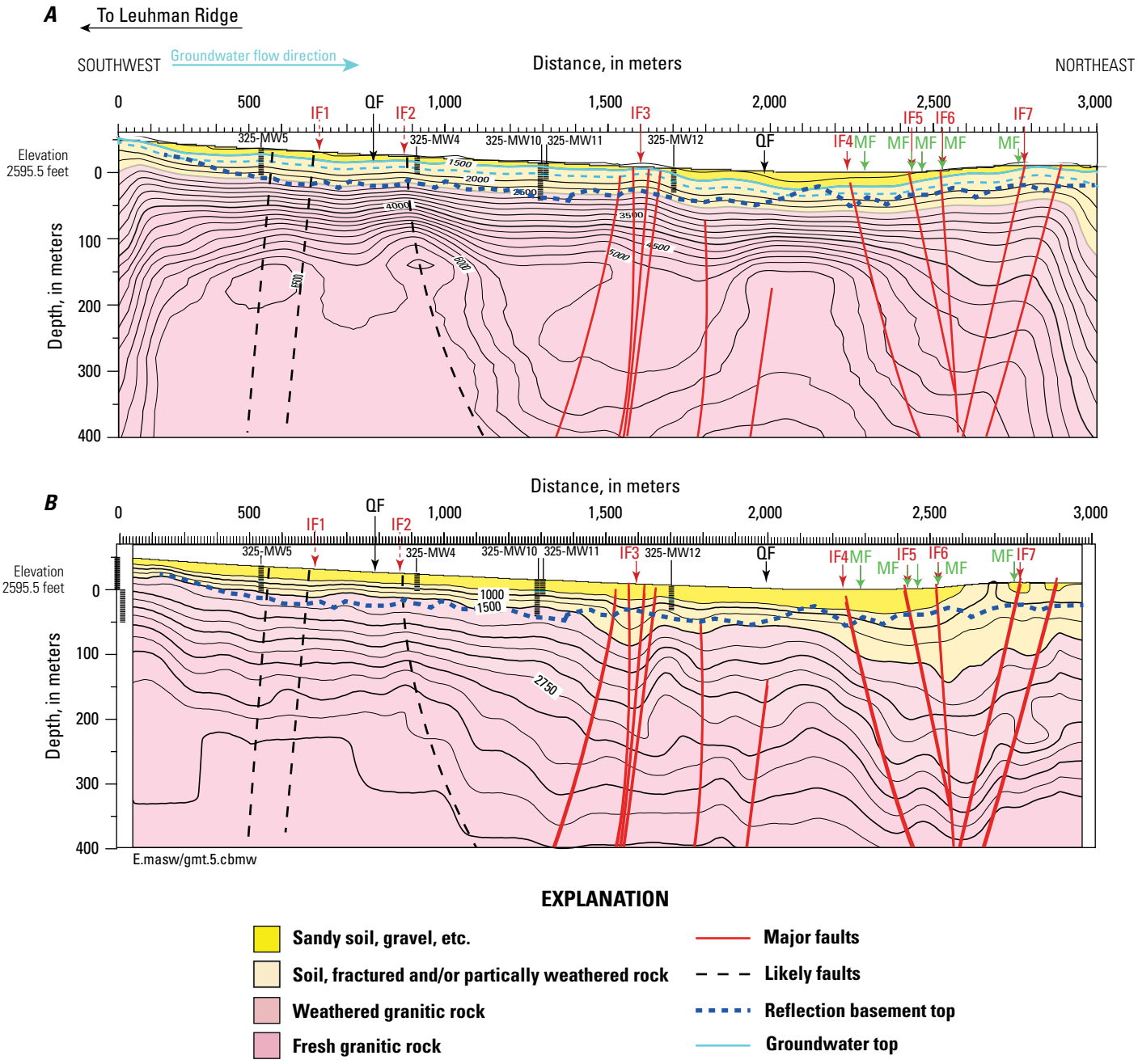

Figure 11. Interpretive cross sections along the Edwards seismic profile, Edwards Air Force Base, California. *A*, Interpretative cross section based on the compressional-wave velocity (v_P) model in figure 3, with contours showing v_P in meters per second (m/s). Faults shown with near-vertical black dashed and solid red lines are interpretative. The near-horizontal dark blue dashed line is the depth of the top of the first strong reflection on figure 8*B* and is interpreted as the top of weathered basement, which approximately follows the 2,500-m/s v_P contour, except at fault zones. The light-blue-colored solid line is the 1,500-m/s v_P contour (top of groundwater), inferred from the lower-resolution model (fig. 3). The light-blue-colored dashed line shows the 1,500-m/s v_P contour (top of groundwater) determined from the higher-resolution model (fig. 4). Locations of wells along the seismic profile are shown as vertical black lines above the surface and horizontal black lines below the surface, with each bar representing 2-meter depth increments. Light-blue-colored bars show depth to the top of groundwater in the wells. Black arrows labeled QF show the surface locations of inferred Quaternary faults (Bryant, 2017). The southwestern and northeastern QFs are referred to as the Leuhman and Spring Faults, respectively, by Bryant (2017). Red arrows labeled IF1 to IF7 show the surface locations of faults interpreted along the profile on the basis of seismic data from this study. Green arrows labeled MF show faults mapped at the surface by Cyr and Miller (2023). *B*, Interpretative cross section based on the shear-wave velocity (v_S) model in figure 5, with contours showing v_S in meters per second. Plotted as in figure 11*A*, but only v_S velocity contours are shown, which do not correlate with groundwater depths.

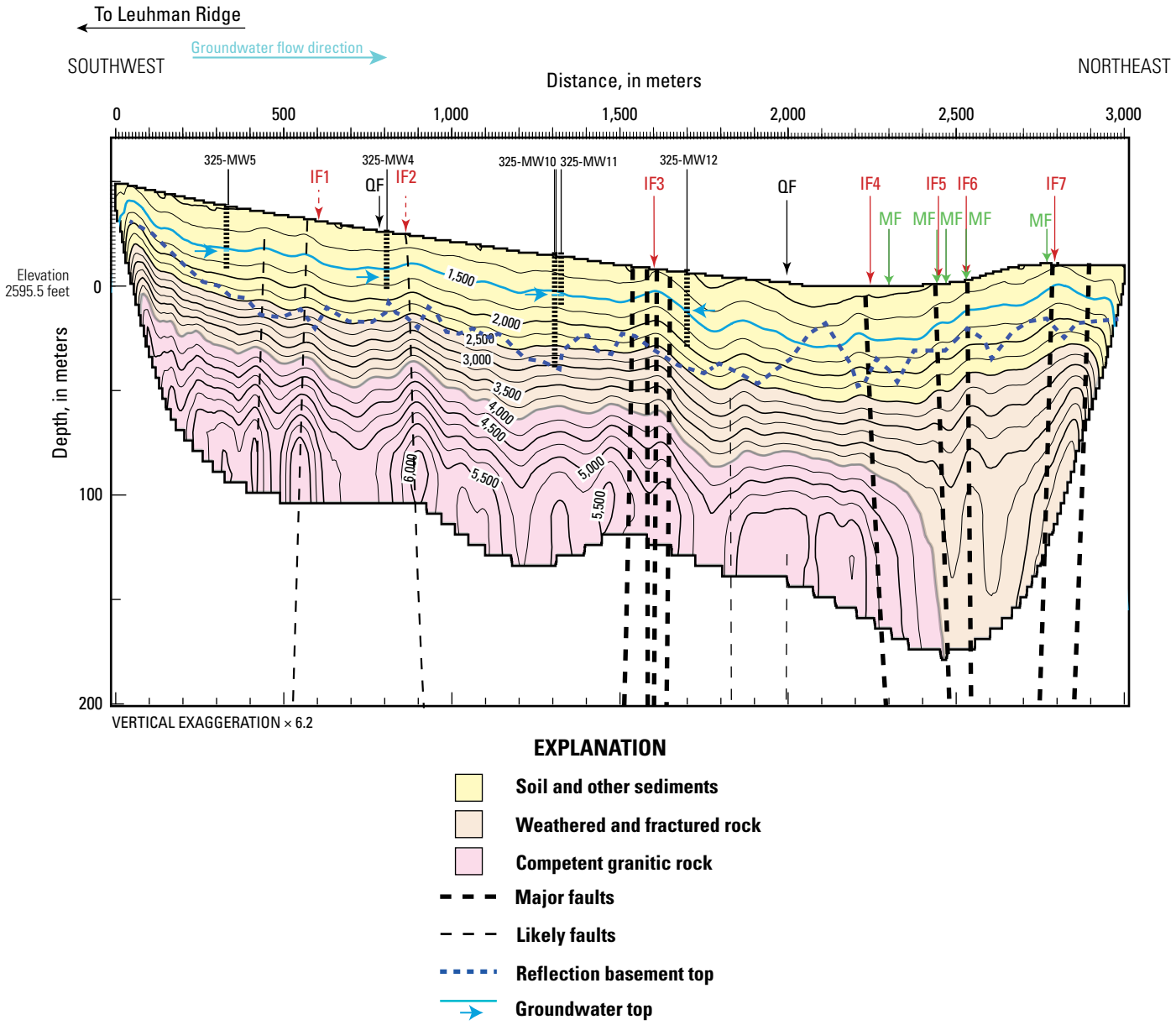

Figure 12. Interpretative cross section based on the compressional-wave velocity (v_P) model (fig. 4) along the Edwards seismic profile, Edwards Air Force Base, California. Near-vertical dashed black lines show interpreted faults shown in figure 11. Red arrows labeled IF1 to IF7 show the surface locations of interpreted faults. Green arrows labeled MF show the locations of faults mapped by Cyr and Miller (2023). Black arrows labeled QF show inferred Quaternary faults mapped by Bryant (2017). The southwestern and northeastern QFs are referred to as the Leuhman and Spring Faults, respectively, by Bryant (2017). Light-blue-colored arrows pointing to bars of the same color represent the depth to groundwater in wells. The 1,500-meter-per-second v_P velocity contour (light-blue-colored contour) from figure 4 correlates with the top of groundwater in wells along the profile. The interpreted top of weathered basement (dashed dark blue line) correlates with the first strong reflection on figure 8*B*.

Regolith: Shallow Sediments, Saprolite, and Highly Weathered Bedrock

Surface geologic mapping along the Edwards seismic profile shows that the surface material consists of various types of alluvium, except near the northeast end of the profile, where weathered granitic rocks are mapped (Cyr and Miller, 2023). We refer to the surface sediments, underlying saprolite, and all materials above the unweathered granitic rocks as regolith (following Holbrook and others, 2014).

The geologic materials closest to the surface along the profile have low velocities (v_p of ~1,000 m/s; v_S of ~500 m/s) and likely correspond to the unconsolidated sediments found along most of the seismic profile. Saprolite and highly weathered granitic rocks likely have higher velocities (Catchings and others, 1999a, b, 2000, 2002; Olona and others, 2010; Holbrook and others,

2014; Kausarian and others, 2014). Both the v_P and v_S models show low velocities (v_P of <2,500 m/s; v_S of <1,500 m/s) that are consistent with those of sediments and saprolite that extend tens of meters deep. On the southwest half of the profile, the top of strong reflections (the reflection basement) approximately correlates with these velocities as well (v_P of 2,500 m/s; v_S of 1,500 m/s) (fig. 11). The thickest sediments lie between distance-meters 1,500 and 2,800 of the seismic profile, but this area also likely includes zones of shallow faulting (figs. 11, 12). The v_S model in particular shows deep zones with v_S <1,500 m/s near distance-meter 1,600 and from distance-meters 2,200 to 3,000. The v_P model, in contrast, does not show such low-velocity zones. Furthermore, the top of strong reflections does not correlate with those velocities in those areas. Thus, the lower v_S in those areas is likely due to zones of water-saturated faulting, which considerably reduces v_S but not v_P.

v_P/v_S ratios can help to further differentiate between sediments and rock. Saturated sediments typically have v_P/v_S ratios of more than 2.0, whereas competent granitic rocks typically have v_P/v_S ratios of much less than 2 (~1.73 or less). Along the Edwards seismic profile, the larger v_P/v_S ratios (2.0 or greater) occur laterally within a thin, near-surface zone (fig. 13) at or just above the top of groundwater (v_P of 1,500 m/s; see figures 6 and 12). Such near-surface, sub-horizontal zones of high v_P/v_S ratios are consistent with saturated, unconsolidated sediments and clays (Stuempel and others, 1984; Catchings and Lee, 1996; Uyanik, 2011; Catchings and others, 2014; Pasquet and others, 2015). The underlying lower values of v_P/v_S ratios (<1.7) likely coincide with highly weathered rock.

Although μ can vary widely among geologic materials, the maximum value of 0.5 correlates with materials that lack a shear modulus, such as fluids or gasses. For sediments, μ can also vary widely depending on water saturation, degree of compaction, and other factors. Along the Edwards seismic profile, μ for shallow-depth (18–22 m) sediments ranges from about 0.35 to more than 0.45 (fig. 14). In some locations, μ is about 0.35 at the surface, likely resulting from unsaturated, unconsolidated sand and other sediments. Overall, μ values along the seismic profile indicate that unsaturated, unconsolidated sediments range in thickness from about 8 to 30 m.

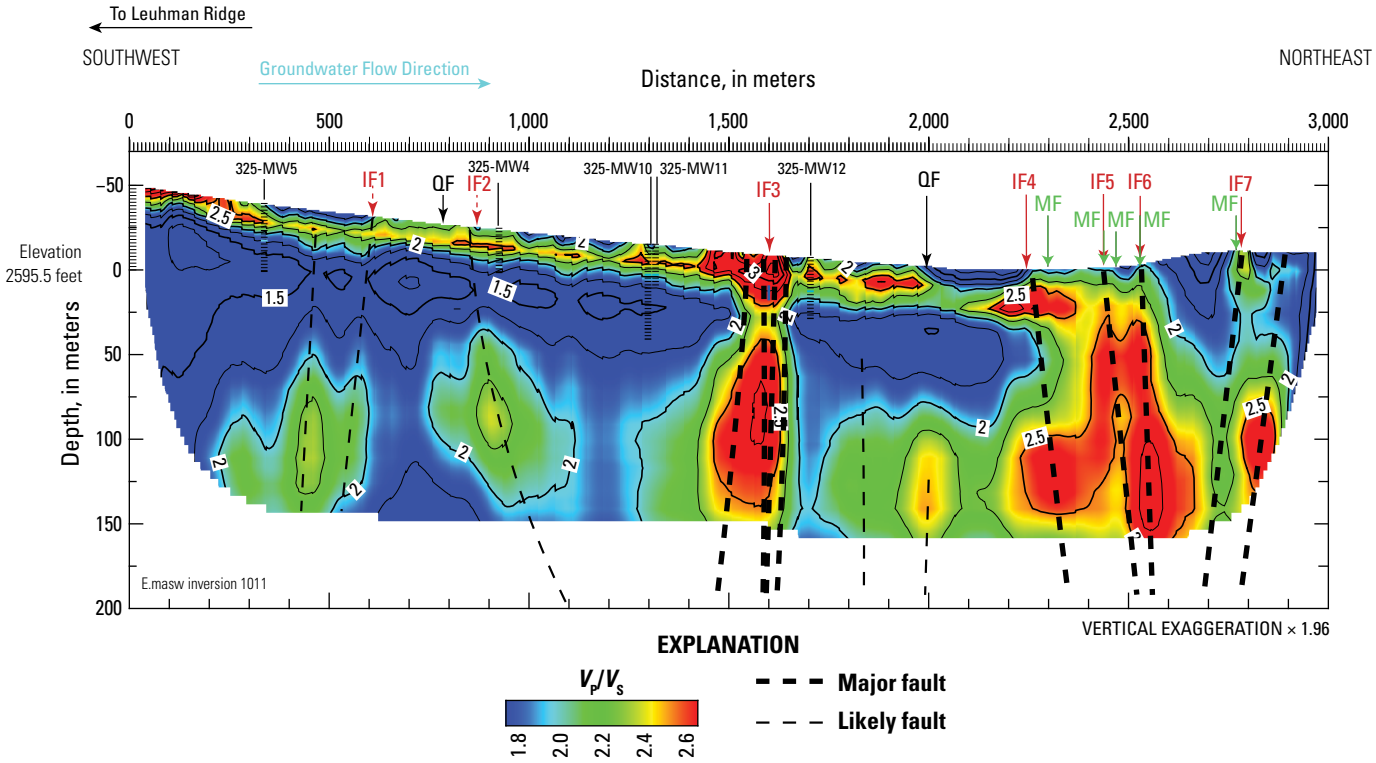

Figure 13. Two-dimensional model of the ratio of compressional-wave velocity to shear-wave velocity (v_P/v_S ratio) along the Edwards seismic profile (Edwards Air Force Base, California), annotated with interpretive faults (dashed black lines) shown in figure 11. Contours show v_P/v_S ratios. The locations of wells along the profile are shown with black vertical lines above the surface and 2-meter-spaced horizontal bars from the surface to the bottom of each well. The depth of groundwater measured in the wells along the seismic profile is shown by light-blue-colored bars at the well locations. Black arrows labeled QF show the surface locations of inferred Quaternary faults (Bryant, 2017). The southwestern and northeastern QFs are referred to as the Leuhman and Spring Faults, respectively, by Bryant (2017). Red arrows labeled IF1 to IF7 show faults interpreted along the profile on the basis of seismic data from this study. Green arrows labeled MF show faults mapped at the surface by Cyr and Miller (2023). Larger version of figure available for download at https://doi.org/10.3133/ofr20231018.

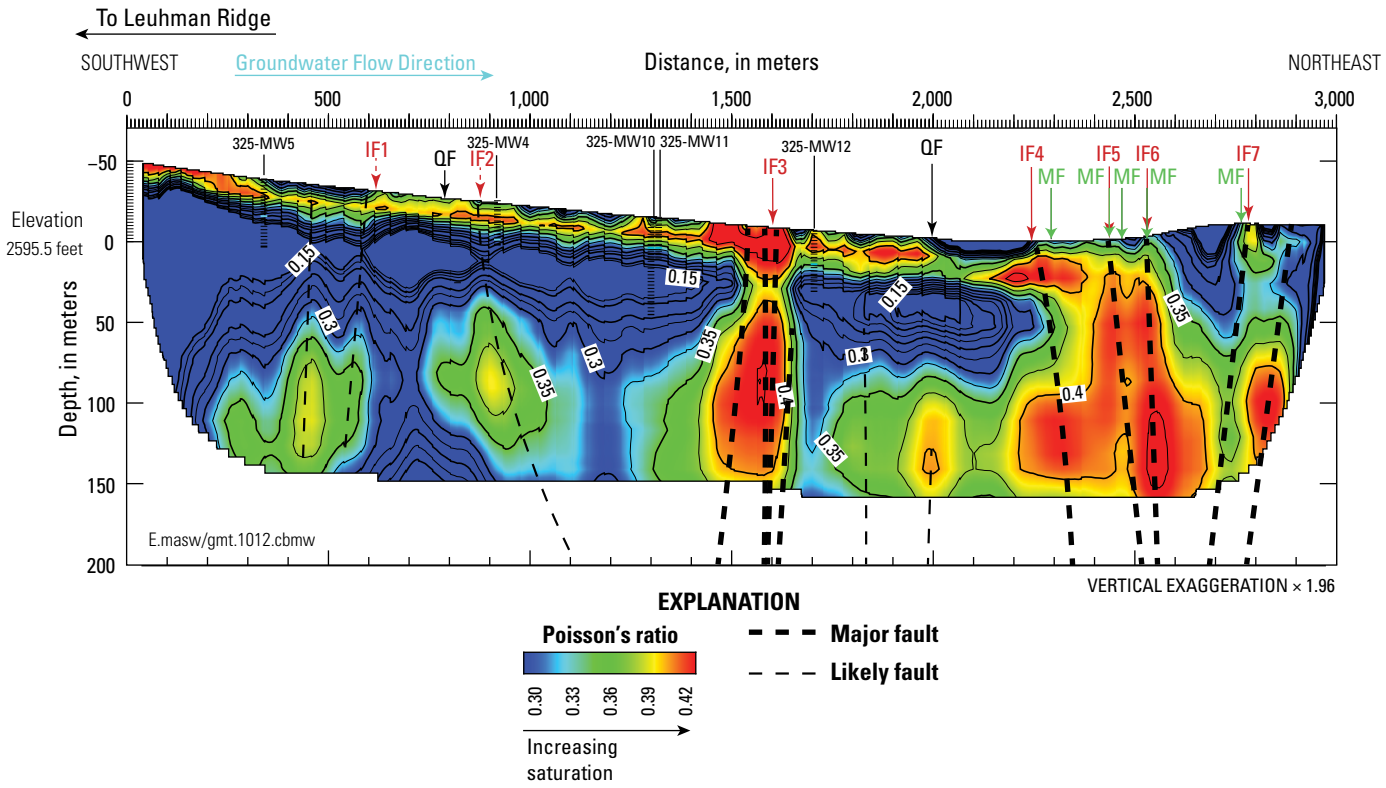

Figure 14. Two-dimensional Poisson's ratio (μ) model along the Edwards seismic profile (Edwards Air Force Base, California), annotated with interpretative faults shown in figure 11. Contours show μ. The locations of wells near the profile are shown with black vertical lines above the surface and 2-meter-spaced horizontal bars from the surface to the bottom of each well. The depth of groundwater measured in the wells along the seismic profile is shown by light-blue-colored bars at the well locations. Black arrows labeled QF show the surface locations of inferred Quaternary faults (Bryant, 2017). The southwestern and northeastern QFs are referred to as the Leuhman and Spring Faults, respectively, by Bryant (2017). Red arrows labeled IF1 to IF7 show faults interpreted along the profile on the basis of seismic data from this study. Green arrows labeled MF show faults mapped at the surface by Cyr and Miller (2023). Larger version of figure available for download at https://doi.org/10.3133/ofr20231018.

Our reflection images show that the shallow subsurface is not strongly reflective in the upper ~40 m (fig. 8*B*) along most of the seismic profile. This shallow, weakly reflective section likely correlates with poorly layered, unconsolidated sediments. Although this observation is consistent with an upper limit of ~40 m for unconsolidated sediments along much of the seismic profile, consolidated sediments may extend to greater depths. The reflection image also indicates that the base of the unconsolidated sediments (top of the weathered basement) does not form a laterally smooth surface (figs. 8, 11, 12).

For most of the Edwards seismic profile, we suggest the regolith (comprising all but pristine granitic basement rocks) consists of lithic units with relatively low velocities (v_P <4,000 m/s; v_S <2,750 m/s) that are locally as deep as 100 m. Along the northeast half of the profile, subsurface lithic units with similar v_P (<4,000 m/s) are as deep as 175 m, and units with similar v_S (<2,750 m/s) are as deep as more than 300 m (fig. 12). However, as discussed in the "Seismic Evidence for Faulting" section, these deep zones of low velocities likely result from faulting, which lowers the seismic velocities of rocks. Such deep zones of low-velocity units are not likely indicative of unconsolidated sediments or sedimentary rocks. We interpret the top of strong reflectors in our reflection image (at ~40 m depth) to correlate with the top of weathered basement along much of the seismic profile, consistent with the idea that the deep (as deep as 300 m), low-v_S (<2,750 m/s) zones do not represent thick sediments, sedimentary rock, or even weathered granite. Instead, faulting and fracturing are likely the cause of the deep zone of low velocities in the northeastern part of the profile.

Shallow-Depth Groundwater Variations

High-resolution v_P refraction tomography is a useful technique to map lateral variations in the top of groundwater within sediments because the v_P of unsaturated sediments is typically less than 1,500 m/s, whereas the v_P of saturated

sediments is at least 1,500 m/s. Many high-resolution v_P refraction tomography studies that include coincident well data or trenches have shown this correlation between the top of groundwater and a v_P of 1,500 m/s (see references in the "Methodology" section). Along the Edwards seismic profile, the depth to groundwater was measured in five nearly coincident wells located along the southwest half of the seismic profile (wells 325-MW04, 325-MW05, 325-MW10, 325-MW11, and 325-MW12) (fig. 9). Water depth measurements for four of the wells were made about 3 months (March 16, 2020) prior to the seismic data acquisition (~June 24, 2020) (Tetra Tech, written communication, 2020; Cromwell and others, 2020). The water depth (22 m) for the fifth well (325-MW05) was recorded in the well's installation report from May 2001. At the time the other four well measurements were taken, static water levels varied between 18 and 22 m below the ground surface. Although the depth to groundwater may have fluctuated during the 3-month period between the well measurements and the seismic data acquisition, the well data still provide a good basis to compare with our v_P tomography indicator of groundwater depth (v_P of 1,500 m/s). In our highest-resolution model, the 1,500-m/s v_P velocity contour approximately correlates with the measured water levels in all five wells (figs. 4, 12). However, the water level in well 325-MW04 is slightly deeper (~3 m) than our v_P = 1,500 m/s contour, but it is within the resolution (grid spacing) of the tomographic model. This 3-m difference also may result from our model resolution.

Well 325-MW04 is also somewhat of an anomaly in another respect. According to the driller's logs (Earth Tech Inc., 2006), weathered bedrock is very shallow (~6 m deep) at well 325-MW04, even though our v_P, v_S, and reflection images are highly inconsistent with weathered rock at such shallow depths, and nearby wells along the seismic profile show weathered rock to be more than 39 m deep (Earth Tech Inc., 2006, p. 4-229). For example, Earth Tech, Inc. (2006) stated that, "Unconsolidated sediments range in thickness from 4 [feet (ft)] in well 325-MW07 to greater than 120 ft (~37 m) in wells 325-MW05 and 325-MW12, where neither weathered nor competent bedrock was encountered." Well 325-MW05 is near well 325-MW04 along the Edwards seismic profile, and it is unlikely that there is more than 30 m difference in the depth to bedrock between the two wells. From other studies in nearby areas of the Mojave Desert, we have found the minimum v_P of weathered granite to be between 2,500 and 3,000 m/s, the v_P of competent granite to be at least 4,000 m/s, the v_S of weathered granite to be about 1,500 m/s, and the v_S of competent granite to be at least 2,700 m/s. However, our modeled v_P and v_S at 6 m depth at well 325-MW04 are <1,250 m/s (fig. 4) and <750 m/s (fig. 5), respectively. Furthermore, there are not strong reflections observed at 6 m depth near well 325-MW04, as would be expected for the top of weathered rock. Thus, we speculate that there may be an error in table B.1-9 of the report (Earth Tech Inc., 2006), or that the borehole may have intersected a large boulder or landslide feature at 6 m depth instead of true weathered basement.

Information about groundwater is inferred from our v_P model, v_P/v_S ratio model, μ model, and reflection image. Based on the 1,500-m/s v_P contour, our model (fig. 4) suggests that the top of groundwater varies from about 8 to 30 m below the ground surface along the seismic profile, with groundwater deepest between distance-meters 1,800 and 2,400 of the seismic profile and shallowest near distance-meter 1,600 and at the northeast and southwest ends of the profile. Importantly, the depth to groundwater (v_P of 1,500 m/s) varies over relatively short lateral distances in places. For example, over an ~200-m-long distance span (distance-meters 1,600–1,800) near the center of the Edwards seismic profile, groundwater (v_P of 1,500 m/s) apparently varies by 18 m in depth.

Our v_P model also helps us to infer the maximum thickness of the alluvial aquifer along the seismic profile. Sediments or weathered rocks with v_P ~2,800 m/s are generally not porous enough to form highly productive aquifers. Along the Edwards seismic profile, the maximum depth of strata with v_P ~2,800 m/s varies laterally but is generally less than 50 m below the ground surface along the southwest half of the seismic profile and as much as 70 m below the ground surface along the northeast half of the seismic profile. However, the lithic units with v_P of ~2,800 m/s at 70 m depth along the northeastern part of the seismic profile are likely not sediments; instead, these deeper (70 m), low-velocity (v_P ~2,800 m/s) units are likely faulted and fractured granitic rocks.

Generally, there is no strong reflector associated with the top of groundwater (v_P of 1,500 m/s) along the Edwards seismic profile, although weak reflectors (relative to basement reflectors) are seen near the top of groundwater (figs. 8*B*, 15). However, there are strong, somewhat laterally continuous reflections (figs. 8*B*, *C*) from the underlying rocks with higher v_P (~3,000 m/s or greater) and v_S (1,500 m/s or greater), particularly along the southwest half of the seismic profile.

Groundwater and Trichloroethylene (TCE) Concentrations

The v_P/v_S ratio model (figs. 6, 13) contains a laterally varying zone where v_P/v_S ratios exceed 2.5 in the upper few tens of meters. This zone of high v_P/v_S ratios is slightly shallower than the top of groundwater in the model, as inferred from the 1,500-m/s v_P contour and the well records along the Edwards seismic profile. At the locations of wells 325-MW10, 325-MW11, and 325-MW12, the model indicates the top of groundwater correlates with v_P/v_S ratios between 2.0 and 2.25, but higher ratios exist just a few meters upward in the section (figs. 6, 13). We observe a similar variation in our μ model (figs. 7, 14). For example, at wells 325-MW10, 325-MW11, and 325-MW12, the top of groundwater (v_P of 1,500 m/s) correlates with a μ of only ~0.35, but at slightly shallower depths, μ values are greater than 0.4, which is closer to values typical of μ for saturated sediments. The difference in depth between the top of groundwater and the depth to the highest ratios may result from depth averaging associated with the MASW method, but our images, nevertheless, show high ratios near the top of groundwater.

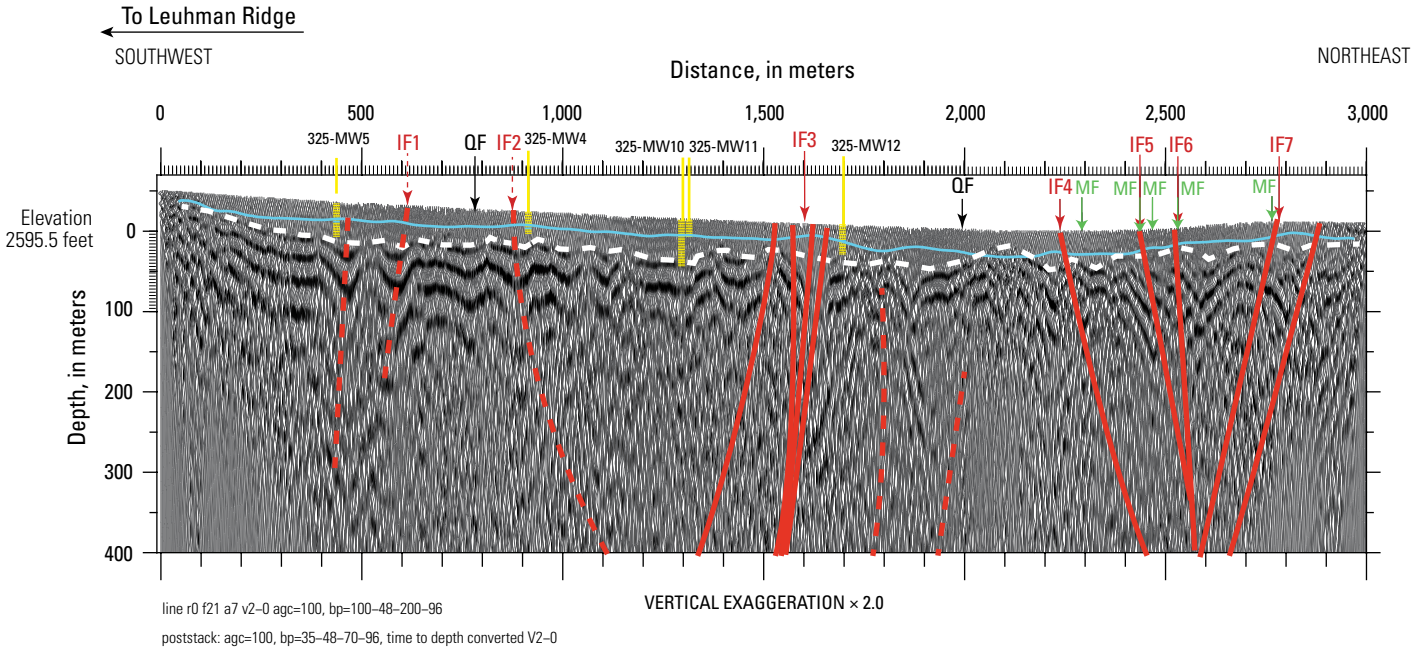

Figure 15. Vertically exaggerated unmigrated reflection image of the upper 400 meters (depth) along the Edwards seismic profile (Edwards Air Force Base, California), annotated with interpreted faults. Solid red lines show major faults, dashed red lines show likely faults. Contours show compressional-wave velocity (v_P). Other annotations show the locations of wells along the seismic profile (yellow), the depth to groundwater as indicated by the 1,500-meter-per-second v_P contour (light blue line), the top of weathered basement rocks (interpreted from the top of the first strong reflector; dashed white line), inferred Quaternary faults from Bryant (2017) (black arrows labeled QF), recently mapped faults from Cyr and Miller (2023) (green arrows labeled MF), and interpreted faults from this study (red arrows labeled IF1 to IF7). The southwestern and northeastern QFs are referred to as the Leuhman and Spring Faults, respectively, by Bryant (2017).

Assuming μ values of more than 0.43 represent saturated sediments (Catchings and others, 2006, 2014), our μ model (figs. 7, 14) indicates the presence of at least partially saturated soils or clay (μ >0.4; v_P/v_S >2.5) at relatively shallow depths (<10 m) along most of the Edwards seismic profile. However, near the center of the profile (approximately spanning distance-meters 1,450–1,600), there appears to be a zone of highly saturated subsurface materials that extends as far as 30 m downward from the surface. This thick zone of elevated μ values and v_P/v_S ratios coincides with the northeast termination of high concentrations (5 to 100 micrograms per liter [µg/L]) of trichloroethylene (TCE) in wells (U.S. Air Force, 2022); wells farther to the northeast (for example, 325-MW12) have concentrations of less than 0.4 µg/L (fig. 10). Because this zone of high μ values and v_P/v_S ratios also extends vertically to the base of our models (~150 m depth) (figs. 7, 14), it indicates that there may be a deep zone of vertical water and contaminant flow at this location, likely along a considerable zone of near-vertical faulting and fracturing.

A zone of high μ values and v_P/v_S ratios also exists at the southwest end of the Edwards seismic profile from the surface to about 10 m deep, but laterally, this zone abruptly pinches out at about meter 400 of the seismic profile, near well 325-MW05 (figs. 13, 14). This zone coincides geographically with an area of higher TCE concentrations (100 µg/L) and even higher TCE concentrations (~1,000 ug/L) slightly northwest of the seismic line (fig. 10). The zone of high ratios along the seismic profile may represent a pediment at the base of Leuhman Ridge that pinches out to the northeast. However, the abrupt termination of high ratios may also represent fault-bounding of sediments near meter 400 of the seismic profile.

Lateral variations in v_P/v_S ratios and μ values in the upper 10–30 m indicate that groundwater flow and TCE concentration is not uniform along the seismic profile; thicker high-ratio zones occur at various locations (figs. 7, 14). We hypothesize that this lack of uniform saturation or groundwater flow may be related to variations in lithology, whereby the aquifer is thicker and consists of more porous materials in discrete locations, or that there are lateral variations in clay content. Alternatively, this segmentation could be due to near-surface faulting, whereby the faults act as groundwater barriers to lateral flow.

Crystalline (Competent) Basement Rock

We interpret the top of unweathered granitic rock to correlate largely with velocity contours as seen in our seismic velocity images (v_S ~2,700 m/s; v_P ~4,000 m/s). As seen elsewhere in California (Zappe, 1979; Catchings and others, 1999a, 2000, 2002; Holbrook and others, 2014), we interpret unweathered or competent granitic basement rock at Edwards AFB to have a minimum v_P of 4,000 m/s, extending to slightly more than 6,000 m/s in the upper 400 m (fig. 3, 11). The v_S of these unweathered basement rocks varies from about 2,700 m/s in the near surface to just over 4,000 m/s at 400 m depth (figs. 5, 11). However, the depth of basement rocks at Edwards AFB cannot be interpreted from seismic velocities alone because of the presence of discrete fault zones, which cause reductions in both v_P and v_S. Reflection imaging, however, provides another indicator of the depths and the physical conditions of basement rocks. Along the southwest half of the Edwards seismic profile, the top of reflective rocks (likely weathered basement) approximately correlates with the 2,500-m/s v_P contour. A deeper, continuous strong reflector (unweathered basement) approximately correlates with the 4,000-m/s v_P contour (figs. 11, 12). On about the northeast third of the seismic profile, neither the 2,500-m/s nor the 4,000-m/s v_P contour correlates with strong reflections; instead, the strong reflectors coincide with lower velocities (figs. 8*D*, 11, 12), which likely result from velocity reductions associated with faulting.

Seismic Evidence for Faulting

P-wave velocity, S-wave velocity, v_P/v_S ratios, μ values, and reflection images, such as those presented in this report, can individually be strong indicators of faulting, but collectively, these images provide excellent evidence of faulting. In this section, we discuss each image in relation to faulting at Edwards AFB.

In the shallow subsurface, a strong indicator of faulting is vertical offsets in the top of groundwater. Faults typically form barriers that affect the lateral flow of groundwater, causing groundwater depths to vary across faults (Proctor, 1968; Wallace and Morris, 1986; Bredehoeft and others, 1992; Catchings and others, 2009, 2014, 2020). Along the Edwards seismic profile, we observe multiple areas where the depth to the top of groundwater (v_P of 1,500 m/s) abruptly changes over relatively short lateral distances (figs. 4, 11, 12). Where mapped faults are observed at the surface on the northeastern part of the Edwards seismic profile (Cyr and Miller, 2023), changes in the depth to the top of groundwater (v_P of 1,500 m/s) in the subsurface correlate with those mapped surface faults. There are also vertical groundwater offsets beneath the alluvial-covered areas, where faults are likely covered at the surface and not obvious from surface mapping. These abrupt changes in groundwater depth along the alluvial-covered areas of the profile, which we interpret as caused by faulting, also coincide geographically with other seismic indicators of faulting.

Another strong indicator of near-vertical faulting in tomographic v_P and v_S images is localized, near-vertical zones of low v_P and v_S. Faulting (shearing) can cause reductions in both v_P and v_S (Nur, 1982), but when faulted rocks are saturated, their P-wave velocity can increase to nearly the same value as that of unfaulted rocks (Nur and Simmons, 1969). S-wave velocity, however, is much less sensitive to saturation, and v_S will be low in faulted rocks whether they are saturated or unsaturated. Thus, on tomographic v_S images, near-vertical fault zones appear as near-vertical zones of low v_S relative to the adjacent unfaulted rocks, but where these fault zones are saturated, they can appear as localized zones of high v_P. As a result, in shallow sediments, near-vertical faults appear as localized, near-vertical zones of relatively low v_S but relatively high v_P. Along the Edwards seismic profile, this inverse relationship between low v_S and high v_P in saturated fault zones occurs at multiple locations and depth ranges, but it is most apparent near distance-meter 1,600 (fig. 11).

If a fault zone is sufficiently saturated at greater depths, localized near-vertical zones of high v_P and low v_S will extend to those greater depths as well, a phenomenon visible along the Edwards seismic profile. Individual faults, appearing as zones of high v_P and low v_S, generally occur within wider overall zones of low v_P and low v_S relative to unfaulted areas; these larger zones can be tens to hundreds of meters wide (fig. 11). Each wide zone of low v_P and v_S occurs because the damage zone caused by individual faults extends beyond both the immediate fault traces and the water ponding areas at individual groundwater barriers (faults). Along the Edwards seismic profile, such wide zones of near-vertical low velocities are seen in competent basement rocks (v_P >4,000 m/s; v_S >2,700 m/s), where v_P and v_S are reduced by as much as 1,000 m/s within the low-velocity zone (LVZ) relative to the adjacent rocks outside the LVZ (for example, see figure 11, distance-meters 2,100–2,800 at 200 m depth). The LVZs also extend to the near surface, as seen in both the v_P and v_S models (fig. 11), and are most conspicuous in three areas along the profile: distance-meters 700–800, distance-meters 1,500–1,700, and distance-meters 2,100–2,800 (figs. 4, 11, 12). Because the v_P and v_S models are derived from differing seismic waves (compressional body waves versus surface waves), the LVZs are not an artifact of modeling. Also, conspicuous LVZs underlie the area where Cyr and Miller (2023) mapped surface faults along the Edwards seismic profile (distance-meters 2,300–2,700) (figs. 9, 11).

High v_P/v_S ratios are perhaps one of the strongest indicators of water-saturated faulting (Catchings and others, 2014) because of the inverse relationship between v_P and v_S in shallow-depth, saturated fault zones. Because v_P is sensitive to water saturation (v_P increases in saturated material) and v_S is sensitive to shearing during the faulting process (v_S decreases with increased shearing), v_P/v_S ratios are elevated in saturated fault zones (Catchings and others, 2014, 2020). The presence of clay minerals, which commonly form during faulting, also elevates v_P/v_S ratios. These observations can be used to identify saturated fault zones, particularly where v_P/v_S ratios are elevated along near-vertical or steeply dipping planes (Catchings and others, 2014).

Several discrete, near-vertical zones of high v_P/v_S ratios exist along the Edwards seismic profile. The most conspicuous zone, which is located between distance-meters ~1,400 and ~1,600, extends from the surface to at least the base of our model (~150 m) (fig. 13). Other near-vertical zones of high v_P/v_S ratios that extend from the surface to the base of the model include those at distance-meters 2,250 and 2,550 and near distance-meter 2,800 (fig. 13), coinciding with surface faults mapped by Cyr and Miller (2023). Several other near-vertical high-v_P/v_S-ratio zones below 50 m depth are near distance-meters 500, 900, and 2,000. All the near-vertical high-v_P/v_S-ratio zones that extend beyond a few tens of meters deep are anomalous, given that these zones extend into competent granitic rock (v_P >4,000 m/s), which typically has v_P/v_S ratios of about 1.6 to 1.8 (Wang and others, 2012) unless saturated, faulted, or both. We observe similar structures in the μ model (fig. 14) that are also consistent with near-vertical faulting along water-saturated zones in the same locations.

Seismic reflection images can present clear evidence of faulting for areas with near-vertical offsets of sub-horizontal layers in the subsurface. On reflection images with sub-horizontally layered strata, faults appear as vertically offset reflectors, especially when there are a series of laterally continuous reflectors that are vertically offset over a range of depths. In addition, for unmigrated reflection images, the vertically offset reflectors often cause vertically aligned diffractions to originate at the intersections of the fault plane and the offset strata. Diffractions appear as upside-down-V-shaped patterns on unmigrated seismic reflection images (figs. 8*A*, 15) and are prominent along much of the Edwards seismic profile. Such zones of near-vertical diffractions are usually associated with faulting (Catchings and others, 2020). Along the Edwards seismic profile, strong diffractions in basement rocks are observed near distance-meters 500, 900, 1,500–1,800, and 2,200–2,800. Abrupt changes in the dips of reflectors can also be strong indicators of faulting in reflection images. Such features are also apparent along the Edwards seismic profile (figs. 8*A*, 15) but are largely masked by diffractive energy in some locations.

In summary, strong indicators of shallow faulting along the Edwards seismic profile include the following co-located features: (1) near-vertical zones of high v_P and low v_S (fig. 11), (2) near-vertical zones of high v_P/v_S ratios (fig. 13), (3) near-vertical zones of high μ (fig. 14), (4) near-vertical zones of offset reflectors and diffractions (fig. 15), (5) near-vertical offsets in the top of groundwater (v_P of 1,500 m/s) (fig. 12), and (6) mapped faults at the surface (fig. 9). On the basis of these multiple seismic observations at the same geographic locations, we suggest several significant fault zones, as well as other smaller faults, exist along the Edwards seismic profile.

Previously mapped surface faults in the study area include the Kramer Hills Fault Zone, which was previously mapped by Jennings (1994), Bortugno (1986), Bryant (2002), and Hart and others (1988). Subsequent additions and revisions to faults present in the study area, excluding the seismically mapped faults presented here, are found in the USGS Quaternary Fault and Fold Database (Bryant, 2017). Also excluded from the USGS Quaternary Fault and Fold Database is the recent mapping by Cyr and Miller (2023), who mapped a zone of faulting near the northeast end of the profile (fig. 9); these faults are labeled MF and shown in green on figures 8, 11, 12, 13, 14, and 15. We independently identified these same faults based on our seismic images (v_P, v_S, v_P/v_S ratios, μ, and reflection images). We also identified a major zone of faulting beneath a relatively thick sequence of sediments near the center of the Edwards seismic profile (distance-meter 1,600) (figs. 11, 12, 13). We labeled these zones of faulting as "interpreted faults" (IP1 to IP7) on figures 8, 11, 12, 13, 14, and 15; these faults likely have important implications for the lateral and vertical flow of groundwater and contaminants across the northeastern area of Edwards AFB. Additionally, the shallow depths of these faults indicate that they may be important for earthquake hazards considerations.

References Cited

Bowles, J.E., 1982, Foundation Analysis and Design (3rd ed.): London, McGraw-Hill, 816 p.

Bortugno, E.J., 1986, Map showing recency of faulting, San Bernardino quadrangle, California, sheet 5 *of* San Bernadino Quadrangle: California Division of Mines and Geology Regional Geologic Map 3A, 5 sheets, scale 1:250,000.

Bredehoeft, J. D., Belitz, K., and Sharp-Hansen, S., 1992, The hydrodynamics of the Big Horn basin—A study of the role of faults: American Association of Petroleum Geologists Bulletin, v. 76, no. 4, p. 530–546.

Brown, E.T., ed, 1981, Rock Characterization, Testing and Monitoring—ISRM Suggested Methods: New York, Pergamon Press, 211 p.

Bryant, W.A., 2003, Mirage Valley, Blake Ranch, and related faults, San Bernardino and Los Angeles counties, *in* Bryant, W.A., and Wong, P., Fault Evaluation Reports Prepared Under the Alquist-Priolo Earthquake Fault Zoning Act—Region 2, southern California: California Geological Survey CD–ROM 2002-02, 1 CD–ROM. [This report is a re-release of California Division of Mines and Geology Fault Evaluation Report 190, released in 1987.]

Bryant, W.A., comp., 2017, Fault number 321, Kramer Hills Fault zone, *in* Quaternary Fault and Fold Database of the United States: U.S. Geological Survey website, accessed May 30, 2023, at https://earthquakes.usgs.gov/hazards/qfaults.

Carmichael, R.S., 1989, Practical handbook of physical properties of rocks and minerals: Boca Raton, Florida, CRC Press, 741 p.

Catchings, R.D., and Lee, W.H.K., 1996, Shallow velocity structure and Poisson's ratio at the Tarzana, California, strong-motion accelerometer site: Bulletin of the Seismological Society of America, v. 86, no. 8, p. 1704–1713, https://doi.org/10.1785/BSSA0860061704.

Catchings, R.D., Goldman, M.R., Lee, W.H.K., Rymer, M.J., and Ponti, D.J., 1998, Faulting apparently related to the 1994 Northridge, California, earthquake, and possible co-seismic origin of surface cracks in Potrero Canyon, Los Angeles County, California: Bulletin of the Seismological Society of America, v. 88, no. 6, p. 1379–1391, https://doi.org/10.1785/BSSA0880061379.

Catchings, R.D., Gandhok, G., Goldman, M.R., Horta, E., Rymer, M.J., Martin, P., and Christensen, A., 1999a, Subsurface, high-resolution, seismic images from Cherry Valley, San Bernardino County, California—Implications for water resources and earthquake hazards: U.S. Geological Survey Open-File Report 99–26, 57 p., https://doi.org/10.3133/ofr9926.

Catchings, R.D., Goldman, M.R., Gandhok, G., Horta, E., Rymer, M.J., Martin, P., and Christensen, A., 1999b, Structure, velocities, and faulting relationships beneath San Gorgonio Pass, California—Implications for water resources and earthquake hazards: U.S. Geological Survey Open-File Report 99–568, 53 p., https://doi.org/10.3133/ofr99568.

Catchings, R.D., Cox, B.F., Goldman, M.R., Gandhok G., Rymer, M.J., Dingler, J., Martin, P., Christensen, A., and Horta, E., 2000, Subsurface structure and seismic velocities as determined from high-resolution seismic imaging in the Victorville, California area—Implications for water resources and earthquake hazards: U.S. Geological Survey Open-File Report 2000–123, 70 p., https://doi.org/10.3133/ofr00123.

Catchings, R.D., Gandhok, G., Goldman, M.R., and Okaya, D., 2001a, Seismic images and fault relations of the Santa Monica Thrust Fault, West Los Angeles, California: U.S. Geological Survey Open-File Report 2001–111, 34 p., https://doi.org/10.3133/ofr01111.

Catchings, R.D., Gandhok, G., and Goldman, M.R., 2001b, Stratigraphic and structural characterization of the OU-1 area at the former George Air Force Base, Adelanto, southern California: U.S. Geological Survey Open-File Report 2001–60, 55 p., https://doi.org/10.3133/ofr0160.

Catchings, R.D., Rymer, M.J., Goldman, M.R., Hole, J.A., Huggins, R., and Lippus C., 2002, High-resolution seismic velocities and shallow structure of the San Andreas Fault zone at Middle Mountain, Parkfield, California: Bulletin of the Seismological Society of America, v. 92, no. 6, p. 2493–2503, https://doi.org/10.1785/0120010263.

Catchings, R.D., Borchers, J.W., Goldman, M.R., Gandhok, G., Ponce, D.A., and Steedman, C.E., 2006, Subsurface structure of the East Bay plain ground-water basin—San Francisco Bay to the Hayward Fault, Alameda County, California: U.S. Geological Survey Open-File Report 2006–1084, 61 p., https://doi.org/10.3133/ofr20061084.

Catchings, R.D., Goldman, M.R., and Gandhok, G., 2007, Structure and velocities of the northeastern Santa Cruz Mountains and the western Santa Clara Valley, California, from the SCSI-LR seismic survey: U.S. Geological Survey Open-File Report 2007–1039, 70 p., https://doi.org/10.3133/ofr20061014.

Catchings, R.D., Gandhok, G., Goldman, M.R., Okaya, D., Rymer, M.J., and Bawden, G.W., 2008, Near-surface location, geometry, and velocities of the Santa Monica fault zone, Los Angeles, California: Bulletin of the Seismological Society of America, v. 98, p. 124–138, https://doi.org/10.1785/0120020231.

Catchings, R.D., Rymer, M.J., Goldman, M.R., and Gandhok, G., 2009, San Andreas Fault geometry at Desert Hot Springs, California, and its effects on earthquake hazards and groundwater: Bulletin of the Seismological Society of America, v. 99, no. 4, p. 2190–2207, https://doi.org/10.1785/0120080117.

Catchings, R.D., Rymer, M.J., Goldman, M.R., Prentice, C.S., and Sickler, R.R., 2013, Fine-scale delineation of the location of and relative ground shaking within the San Andreas Fault zone at San Andreas Lake, San Mateo County, California: U.S. Geological Survey Open-File Report 2013–1041, 53 p., https://doi.org/10.3133/ofr20131041.

Catchings, R.D., Rymer, M.J., Goldman, M.R., Sickler, R.R., and Criley, C.J., 2014, A method and example of seismically imaging near-surface fault zones in geologically complex areas using Vp, Vs, and their ratios: Bulletin of the Seismological Society of America, v. 104, no. 4, p. 1989–2006, https://doi.org/10.1785/0120130294.

Catchings, R.D., Dixit, M.M., Goldman, M.R., and Kumar, S., 2015, Structure of the Koyna-Warna Seismic Zone, Maharashtra, India—A possible model for large, induced earthquakes elsewhere: Journal of Geophysical Research, v. 120, no. 5, p. 3479–3506, https://doi.org/10.1002/2014JB011695.

Catchings, R.D., Goldman, M.R., Chan, J.H., Sickler, R.R., Rymer, M.J., and Criley, C.J., 2020, Seismic evaluation of shallow-depth structure, faulting, and groundwater variations across the Dos Palmas Preserve, Riverside County, California: U.S. Geological Survey Open-File Report 2019–1130, 21 p., https://doi.org/10.3133/ofr20191130.

Christensen, A.H., Siade, A.J., Martin, P., Langeheim, V.E., Catchings, R.D., and Burgess, M.K., 2015, Feasibility and potential effects of the proposed Amargosa Creek recharge project, Palmdale, California: U.S. Geological Survey Scientific Investigations Report 2015–5054, 48 p., https://doi.org/10.3133/sir20155054.

Cromwell, G., Fenton, N.C., and Ely, C.P., 2020, Select borehole data for Edwards Air Force Base and vicinity, Antelope Valley, CA: U.S. Geological Survey data release, https://doi.org/10.5066/P90N3MQQ.

Cyr, A.J., and Miller, D.M., 2023, Preliminary surficial geologic map of Leuhman Ridge and the surrounding area, Edwards Air Force Base and Air Force Research Laboratory, Kern and San Bernardino Counties, California: U.S. Geological Survey Open-File Report 2023–1014, 1 sheet, scale 1:18,000, 15-p. pamphlet, https://doi.org/10.3133/ofr20231014.

Dibblee, T.W., Jr., 1967, Areal geology of the western Mojave Desert, California: U.S. Geological Survey Professional Paper 522, 161 p., https://doi.org/10.3133/pp522.

Earth Tech Inc., 2006, Environmental restoration program remedial investigation summary report, East Air Force Research Laboratory, Operable Unit 9, Edwards Air Force Base, California: Edwards Air Force Base Administrative Record File 1662, 501 p.

Fumal, T.E., 1978, Correlations between seismic wave velocities and physical properties of near-surface geologic materials in the southern San Francisco Bay region, California, U.S. Geological Survey Open-File Report 78–1067, 123 p., https://doi.org/10.3133/ofr781067.

Gandhok, G., Catchings, R.D., Goldman, M.R., Horta, E., Rymer, M.J., Martin, P., and Christensen, A., 1999, High-resolution seismic reflection/refraction imaging from Interstate 10 to Cherry Valley Boulevard, Cherry Valley, Riverside County, California—Implications for water resources and earthquake hazards: U.S. Geological Survey Open-File Report 99–320, 58 p., https://doi.org/10.3133/ofr99320.

Goldman, M.R., Catchings, R.D., Chan, J.H., Criley, C.J., and Sickler, R.R., 2021, Data release for a 2020 high-resolution seismic survey across northeastern Edwards Air Force Base, Kern County, California: U.S. Geological Survey data release, https://doi.org/10.5066/P9ZAM79S.

Hart, E.W., Bryant, W.A., Kahle, J.E., Manson, M.W., and Bortugno, E.J., 1988, Summary report—Fault evaluation program, 1986-1987, Mojave Desert region and other areas: California Division of Mines and Geology Open-File Report 88-1.

Hayashi, K., 2008, Development of surface-wave methods and its application to site investigations: Kyoto, Kyoto Prefecture, Kyoto University, Ph.D. Dissertation, 278 p., https://doi.org/10.14989/doctor.k13774.

Hayashi, K., and Suzuki, H., 2004, CMP cross-correlation analysis of multi-channel surface-wave data: Exploration Geophysics, v. 35, no. 1, p. 7–13, https://doi.org/10.1071/EG04007.

Holbrook, W.S, Riebe, C.S., Elwaseif, M., Hayes, J.L., Basler-Reeder, K., Harry, D.L., Malazian, A., Dosseto, A., Hartsough, P.C., and Hapmans, J.W., 2014, Geophysical constraints on deep weathering and water storage potential in the Southern Sierra Critical Zone Observatory: Earth Surface Processes and Landforms, v. 39, no. 3, p. 366–380, https://doi.org/10.1002/esp.3502.

Hole, J.A., 1992, Nonlinear high-resolution three-dimensional seismic travel time tomography: Journal of Geophysical Research, v. 97, no. B5, p. 6553–6562, https://doi.org/10.1029/92JB00235.

Jennings, C.W., 1994, Fault activity map of California and adjacent areas with location and ages of recent volcanic eruptions: California Division of Mines and Geology California Geologic Data Map 6, 1 sheet, scale 1:750,000.

Kausarian, H., Shamsudin, A.R., and Yuskar, Y., 2014, Geotechnical and rock mass characterization using seismic refraction method at Kajang Rock Quarry, Semenyih, Selangor Darul Ehsan: Journal of Ocean, Mechanical, and Aerospace Science and Engineering, v. 13, p. 12–17, accessed May 10, 2022, at https://isomase.org/JOMAse/Vol.13%20Nov%202014/13-3.pdf.

Olona, J., Pulgar, J.A., Fernández-Viejo, G., López-Fernández, C., and González-Cortina, J.M., 2010, Weathering variations in a granitic massif and related geotechnical properties through seismic and electrical resistivity methods: Near Surface Geophysics, v. 8, p. 585–599, https://doi.org/10.3997/1873-0604.2010043.

Nur, A., 1982, Wave propagation in porous rocks: Stanford Rock Physics Progress Report, v. 13, Stanford, California, Stanford Department of Geophysics, School of Earth Sciences, 121 p.

Nur, A., and Simmons, G., 1969, The effect of saturation on velocity in low porosity rocks: Earth and Planetary Science Letters, v. 7, no. 2, p. 183–193, https://doi.org/10.1016/0012-821X(69)90035-1.

Pasquet, S., Bodet, L., Dhemaied, A., Mouhri, A., Vitale, Q., Rejiba, F., Flipo, N., and Guerin, R., 2015, Detecting different water table levels in a shallow aquifer with combined P-, surface and SH-wave surveys—Insights from Vp/Vs or Poisson's ratios: Journal of Applied Geophysics, v. 113, p. 38–50, https://doi.org/10.1016/j.jappgeo.2014.12.005.

Proctor, R.J., 1968, Geology of the Desert Hot Springs-Upper Coachella Valley Area, California (with a selected bibliography of the Coachella Valley, Salton Sea, and vicinity): California Division of Mines and Geology Special Report 94, 43 p., https://doi.org/10.2172/884810.

Rosa, C.M., Catchings, R.D., Rymer, M.J., Grove, K., and Goldman, M.R., 2016, Structure of the 1906 near-surface rupture zone of the San Andreas Fault, San Francisco Peninsula segment, near Woodside, California: U.S. Geological Survey Open-File Report, 2016–1063, 35 p., https://doi.org/10.3133/ofr20161063.

Salem, H.S., 2000, Poisson's ratio and the porosity of surface soils and shallow sediments, determined from seismic compressional and shear wave velocities: Geotechnique, v. 50, no. 4, p. 461–463, https://doi.org/10.1680/geot.2000.50.4.461.

Sowers, T., and Boyd, O.S., 2019, Petrologic and mineral physics database for use with the USGS National Crustal Model: U.S. Geological Survey data release, https://doi.org/10.5066/P9HN170G.

Stüempel, H., Kähler, S., Meissner, R., and Milkereit, B., 1984, The use of seismic shear waves and compressional waves for lithological problems of shallow sediments: Geophysical Prospecting, v. 32, no. 4, p. 662–675, https://doi.org/10.1111/j.1365-2478.1984.tb01712.x.

Thomsen, L.,1990, Poisson was not a geophysicist!: The Leading Edge, v. 9, no. 12, p. 27–29, https://doi.org/10.1190/1.1439706.

U.S. Air Force, 2022, 2019 Groundwater Monitoring Report, Northeast Air Force Research Laboratory Groundwater Area, Operable Unit 4/9, Edwards Air Force Base, California: Edwards Air Force Base, California, Air Force Civil Engineer Center, 2318 p., accessed February 27, 2023, at https://documents.geotracker.waterboards.ca.gov/esi/uploads/geo_report/7415972709/DOD100111600.PDF.

Uyanik, O., 2011, The porosity of saturated shallow sediments from seismic compressional and shear wave velocities: Journal of Applied Geophysics, v. 73, no. 1, p. 16–24.

Wallace, R.E., and Morris, H.T., 1986, Characteristics of faults and shear zones in deep mines: Pure Applied Geophysics, v. 124, nos. 1–2, p. 107–125, https://doi.org/10.1007/BF00875721.

Wang, X.-Q., Schubnel, A., Fortin, J., David, E.C., Guéguen, Y., and Ge, H.-K., 2012, High Vp/Vs ratio—Saturated cracks or anisotropy effects?: Geophysical Research Letters, v. 39, article L11307, https://doi.org/10.1029/2012GL051742.

Zappe, S.O., 1979, In situ seismic velocities of granitic rocks, Mojave Desert, California: Riverside, California, University of California, Riverside, M.S. thesis, 145 p.

Zhu, F., Gibson, R.L., Jr., Watkins, J.S., and Yuh, S.H., 2000, Distinguishing water saturation changes from porosity or clay content changes using multicomponent seismic data: Gulf Coast Association of Geological Societies Transactions, v. 50, p. 249–258.

Appendix. One-Dimensional Velocity Models for the Edwards Seismic Profile, Edwards Air Force Base, California

One-dimensional (1D) velocity-depth functions are often used by seismologists and engineers for various purposes, particularly 1D shear-wave velocity (v_S) models. Here, we present 1D models for the shallow, high-resolution, compressional-wave velocity (v_P) model (figure 1.1), the deeper v_P model (figure 1.2), and the v_S model (figure 1.3) presented in this report. One-dimensional models are shown at meters 500, 1,000, 1,500, 2,000, and 2,500 along the Edwards seismic profile.

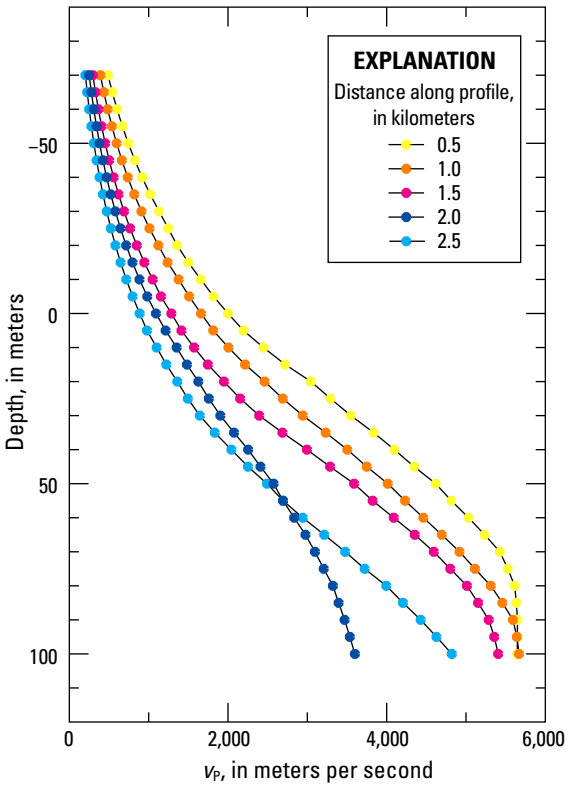

Figure 1.1. One-dimensional compressional-wave velocity (v_P) models at 500-meter (m) distance intervals along the Edwards seismic model shown in figure 4 of this report. The colored dots represent velocity measurements at 3-m depth intervals. The black lines show interpolations between the individual measured velocities.

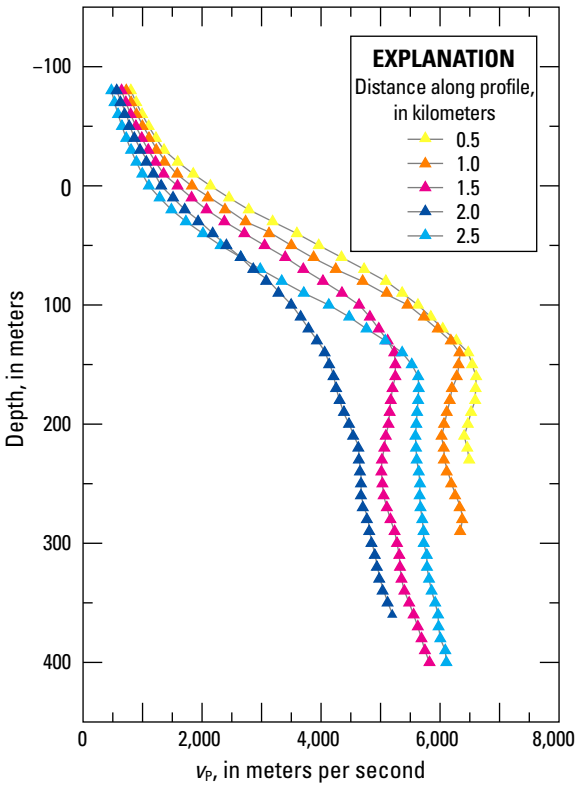

Figure 1.2. One-dimensional compressional-wave velocity (v_P) models at 500-meter (m) distance intervals along the Edwards seismic model shown in figure 3 of this report. The colored triangles represent velocity measurements at 10-m depth intervals. The black lines show interpolations between individual measured velocities.

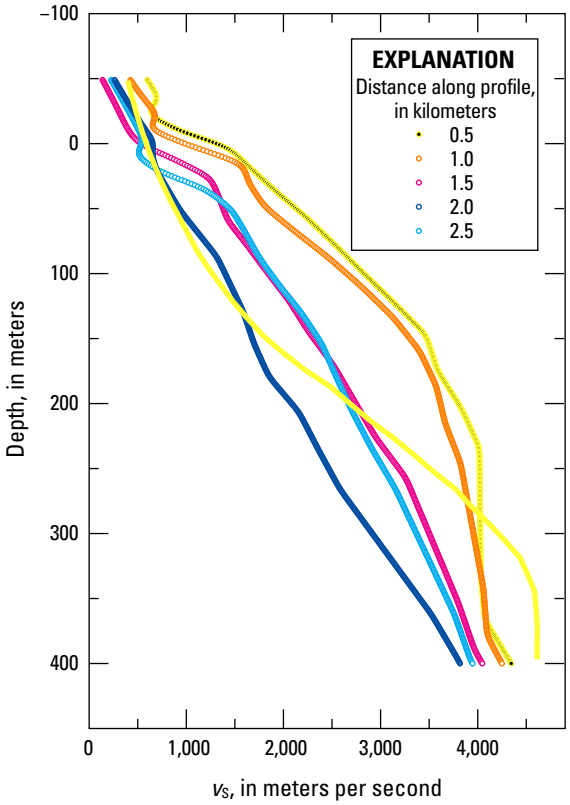

Figure 1.3. One-dimensional shear-wave-velocity (v_S) models at 500-meter (m) distance intervals along the Edwards seismic model shown in figure 5 of this report. The colored circles represent velocity measurements at 1-m depth intervals.

Moffet Field Publishing Service Center
Manuscript approved February 22, 2023
Edited by Claire Ashcraft
Layout by Cory Hurd

ISSN 2331-1258 (online)
https://doi.org/10.3133/ofr20231018